JCI insight

SRF deletion results in earlier disease onset in a mouse model of amyotrophic lateral sclerosis

Jialei Song, … , Francesco Roselli, Bernd Knöll

JCI Insight. 2023. https://doi.org/10.1172/jci.insight.167694.

Research In-Press Preview Neuroscience

Graphical abstract

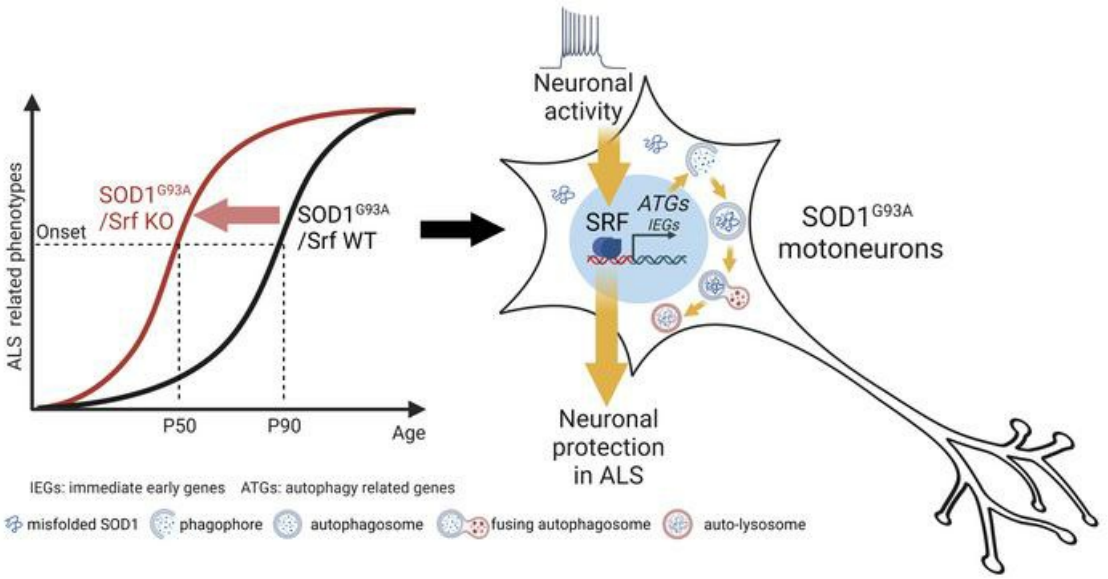

SRF deletion results in earlier disease onset in a mouse model of amyotrophic lateral sclerosis

Short title: SRF deletion accelerates ALS progression in the SOD1 mouse model

Jialei Song[1,2,#], Natalie Dikwella[1,2,#], Daniela Sinske[1], Francesco Roselli[2,3]* and Bernd Knöll[1]*

[1]Institute of Neurobiochemistry
Ulm University
Albert-Einstein-Allee 11
89081 Ulm
Germany

[2] Department of Neurology
Ulm University
89081 Ulm
Germany

[3] German Center for Neurodegenerative Diseases (DZNE)-Ulm
89081 Ulm
Germany

*shared corresponding authors

bernd.knoell@uni-ulm.de

phone: 0040 731 500 338 30

francesco.roselli@uni-ulm.de

phone 0049 731 500 63147

[#]both authors equally contributed

The authors have declared that no conflict of interests exist.

Keywords: ALS/autophagy/motoneuron/SOD1/SRF

Abstract

Changes in neuronal activity modulate the vulnerability of motoneurons (MNs) in neurodegenerative diseases including amyotrophic lateral sclerosis (ALS). So far, the molecular basis of neuronal activity's impact in ALS is poorly understood. Herein we investigated the impact of deleting the neuronal activity stimulated transcription factor (TF) serum response factor (SRF) in MNs of $SOD1^{G93A}$ mice. SRF was present in vulnerable MMP9 positive MNs. Ablation of SRF in MNs induced an earlier disease onset starting around 7-8 weeks after birth, as revealed by enhanced weight loss and decreased motor ability. This earlier disease onset in SRF depleted MNs was accompanied by a mild elevation of neuroinflammation and neuromuscular synapse degeneration, whereas overall MN numbers and mortality were unaffected. In SRF deficient mice, MNs showed impaired induction of autophagy encoding genes suggesting a new SRF function in transcriptional regulation of autophagy. Complementary, constitutive-active SRF-VP16 enhanced autophagy encoding gene transcription and autophagy progression in cells. Furthermore, SRF-VP16 decreased ALS-associated aggregate induction. Chemogenetic modulation of neuronal activity uncovered SRF as important TF mediating activity-dependent effects, which might be beneficial to reduce ALS disease burden. Thus, our data identifies SRF as a new gene regulator connecting neuronal activity with the cellular autophagy program initiated in degenerating MNs.

Introduction

Motoneurons (MNs) display differences in vulnerability to the pathogenic process determining Amyotrophic Lateral Sclerosis (ALS). While fast-fatigable MNs (FF-MN) and large fatigue-resistant MNs (FR-MN) are highly affected and are the first to degenerate, small FR-MN and slow MN (S-MN) are resistant and degenerate only in part and only at the end-stage (1-4). Considering that FF-MN and S-MN differ in their basic firing properties (5), as well as in their transcriptional profile (6, 7), it has been hypothesized that differences in excitability and MN activity may account for the differential vulnerability (8). Furthermore, only vulnerable FF-MNs and large FR-MNs express matrix metalloproteinase-9 (MMP9) as a marker (2). Whether MN hyper- or hypo-excitability is associated with vulnerability is currently under debate. Early observations indicated that MNs are hyperexcitable in ALS, which contributes to their slow excitotoxic death (9-12). More recent work has shown that vulnerable, FF-MNs display hypoexcitability before denervation (13-15), whereas S-MNs remain hyperexcitable (3). Similar changes in excitability have been observed in iPSC (induced pluripotent stem cell)-derived MNs with different mutations (16, 17). Here, MNs show early signs of increased excitability, but a decrease in excitability over time. Interestingly, restoration of excitation through chemogenetics appears to have a beneficial effect on multiple ALS associated cellular phenotypes including autophagy impairment, protein aggregation, ER stress and neuromuscular junction denervation (17-20). In addition to these modifications of intrinsic excitability (13), disruption of synaptic inputs has been also reported in MNs (19, 20). These observations suggest that during disease progression, vulnerable MNs shift from a stage of increased excitability to one of decreased excitability, which contributes to the loss of this MN subpopulation. However, the molecular pathway(s) linking MN excitation to their vulnerability are not well described (20).

Synaptic transmission induces activity-dependent gene expression involved in the remodeling of neuronal responses in development, memory, learning and repair (21, 22). The Serum Response Factor (SRF) is one of the key transcription factors (TFs) of neuronal activity dependent gene expression (23, 24). In conjunction with co-regulators of the TCF (e.g. Elk1) and MRTF (e.g. MRTF-A) family, SRF is responsible for the induction of immediate early genes (IEG) such as Fos (*c-Fos, Fosb*) and Egr (*Egr1, Egr2, Egr3*) family members, *Arc* and *Npas4* (25, 26) during periods of increased synaptic activation. Neuronal activity targeting SRF can be elicited by ocular dominance plasticity (27), novel environments (28), drug application (29), acute stress (30, 31) and epileptic seizures (25, 26). For instance, IEG induction by epileptic seizures is diminished in brain-specific *Srf* mutant mice (25, 26).

SRF conveys neuroprotection in several neurodegenerative paradigms. In facial MNs, constitutively-active SRF-VP16 protects from degeneration after injury (32) and enhances nerve regeneration (33). Similarly, SRF mediates neuroprotection against oxidative stress (34), DNA damage (35) and traumatic brain injury (36). Thus, the transcriptional programs driven by SRF appear to increase neuronal resilience to insults (32, 35). This suggests that SRF is a promising candidate that simultaneously links intrinsic neuronal excitability and synaptic inputs, as well as the dysfunction of cellular processes and MN degeneration observed in ALS. However, the role of SRF in ALS has not yet been analyzed.

In order to analyze a potential neuroprotective SRF function in ALS, we engineered a conditional *Srf* mouse mutant in the context of the SOD1^{G93A} ALS model where SRF was deleted in MNs. We have demonstrated that SRF removal from MNs determines an earlier disease appearance and an accelerated disease course with no difference in overall survival. We provide a new link for SRF as a gene regulator connecting neuronal-activity mediated gene expression with autophagy induction in MNs with an ALS pathology.

Results

SRF is present in vulnerable mouse and human MNs

First, we explored SRF expression across vulnerable and non-vulnerable MNs in WT and SOD1^{G93A} mice (henceforth mSOD1) in the lumbar (L3-L5) spinal cord (Figure 1). Corresponding to the presymptomatic and early symptomatic stages (37), we focused on the timepoints P50 and P90, respectively. Sections were immunostained for SRF together with ChAT (marker of all MNs) and MMP-9 (2, 15). SRF displayed a strong nuclear MN immunolocalization in both genotypes, with more than 50% of MNs displaying SRF immunostaining at P50 (Figure 1A, B and G). However, at P90 (Figure 1C, D) – a time point after which degeneration of MN subpopulations has already occurred – a decrease in SRF^{+} MNs was observed in mSOD1 compared to WT mice (Figure 1G). Besides MNs (blue in Fig. 1A-F), SRF was also present in ChAT and VAChT negative neurons (green only in Fig. 1A-F).

Next, we analyzed SRF expression in vulnerable (MMP9^{+}) and non-vulnerable (MMP9^{-}) MNs at both P50 and P90 (Figure 1H). Here, approximately 60% of vulnerable and 40% of resistant MNs (MMP9^{-}) were SRF positive (Figure 1H). The number of vulnerable and non-vulnerable SRF positive neurons was comparable in the WT mice (P50; Figure 1G, H). However, in mSOD1 mice, more vulnerable neurons were SRF positive (approx. 70%; Figure 1H). At P90 (Figure 1C, D), a decrease in SRF^{+} vulnerable MNs was observed in mSOD1 mice compared to P50 (Figure 1H). This down-regulation between P50 and P90 was not observed to the same extent in WT mice (Figure1H).

In addition to mouse MNs, we analyzed the expression of SRF and its cofactor MRTF-A in MNs of sporadic human ALS cases (Supp. Figure 1, Supp. Table 1). In MNs of control cases, approximately 50% of all MNs had either nuclear SRF or MRTF-A localization (Supp. Figure 1). In ALS patient-derived sections, we observed a lower number of SRF positive neurons,

with approximately 20% of MNs being SRF positive (Supp. Figure 1M). Although rarely observed in the less severe and later affected thoracic MNs of ALS cases, we identified a subpopulation of surviving MNs in the lumbar sections (up to 60%) displaying atypical nuclear SRF localization (Supp. Figure 1N). These neurons revealed a rod-like or aggregated SRF nuclear morphology in contrast to the uniform SRF expression observed in control MNs (Supp. Figure 1C vs. F). Conversely, no differences for MRTF-A between healthy samples and ALS specimens were observed (Supp. Figure 1).

Taken together, SRF is present in both vulnerable rodent and human MNs and a disruption of uniform SRF nuclear localization may potentially be occurring in human ALS MNs.

SRF deletion in MNs results in earlier disease onset in the SOD1 mouse model

In order to investigate whether SRF executes a critical role in the vulnerability of MN subpopulations, we removed SRF from MNs in the context of the ALS-related $SOD1^{G93A}$ mutation. First, $Srf^{loxp/loxp}$ mice were bred with $ChAT^{Cre}$ mice to obtain a line in which SRF was selectively deleted from MNs (and other cholinergic cells, see methods). The resulting $Srf^{loxp/loxp;\ ChAT\text{-}Cre}$ mice (henceforth called Srf KO) were viable and did not display any obvious phenotype. Subsequently, female $Srf^{loxp/loxp;\ ChAT\text{-}Cre}$ mice were bred with male mSOD1 mice, resulting in $hSOD1^{G93A}/Srf^{loxp/loxp;\ ChAT\text{-}Cre}$ offspring (henceforth referred to as mSOD1/Srf KO). These mice were viable, but were born at a frequency slightly lower than the expected mendelian rate of 6.25% (male: 4,74% and female 1,25%). SRF expression was abolished in MNs of the Srf KO mice, but was detectable in non-MN cells of the spinal cord (Figure 1E, F and I). The efficiency of SRF ablation at P90 was identical in Srf KO and mSOD1/Srf KO animals (Figure 1I). At P50 and P90, down-regulation of SRF mediated gene expression was

confirmed by a reduction in the SRF target gene c-Fos in MNs of mSOD1/Srf KO compared to mSOD1 mice (Supp. Fig. 2). It is worth noting that the number of c-Fos positive MNs was induced in mSOD1 mice compared to WT (Supp. Figure 2). Furthermore, vulnerable MMP9 positive MNs co-localized more frequently with c-Fos compared to MMP9 negative MNs in mSOD1 mice (Supp. Figure 2).

We subjected mice of the four genotypes (WT, Srf KO, mSOD1 and mSOD1/Srf KO) to an initial behavioral assessment (exploratory cohort, Supp. Figure 3), with body-weight and grip strength measured separately in males and females. Interestingly, we found that male mSOD1/Srf KO had a significantly lower body-weight and reduced grip strength at P63 and P70-77 than mSOD1 mice, implying a deterioration of the disease upon SRF loss in MNs.

These findings prompted us to explore the clinical, motor and behavioral phenotype in a second, independent group of mice (in-depth cohort; Figures 2 and 3). Respectively, the animal numbers in the exploratory and in-depth cohort were, as follows: for females 14 + 8 WT, 10 + 9 Srf KO, 14 + 9 mSOD1 and 11 + 3 mSOD1/Srf KO and for males 13 + 9 WT, 8 + 8 Srf KO, 8 + 12 mSOD1 and 8 + 6 mSOD1/Srf KO animals. The reduced mendelian frequency obtained for female mSOD1/Srf KO mice (see above) resulted in the inclusion of fewer female compared to male animals. To analyze the in-depth cohort, we considered multiple ALS associated phenotypes including the neurological score and body-weight (37, 38), grip strength, inverted grid and pole test (Figs. 2 and 3) and overall survival (Figure 3). Since there is a substantial sex effect in ALS (39), male and female mice were investigated separately.

In the in-depth cohort (Figs. 2 and 3), male SOD1 animals exhibited a plateau in weight gain at the age of 10 weeks, followed by a subsequent decline in weight starting around 13-14 weeks (Figure 2A). In contrast, WT and Srf KO groups displayed steady weight gain (Figure 2A). Interestingly, male mSOD1/Srf KO mice stopped gaining weight before the mSOD1 mice,

reached a lower peak body-weight and started losing weight already at 8-9 weeks (Figure 2A). In contrast to males, there was no obvious difference in the body weight of mSOD1/Srf KO females when compared to the SOD1 females (Figure 2B).

mSOD1 and mSOD1/Srf KO mice also showed differences in their NeuroScore assessments (37, 40). Male mSOD1 mice became symptomatic (NeuroScore 1) at around 12-13 weeks of age and reached a maximum severity score of 2.5 by week 20 (Figure 2C). In contrast, mSOD1/Srf KO mice reached NeuroScore 1 much earlier at eight weeks and NeuroScore 3 at 16 weeks (Figure 2C). Furthermore, the NeuroScore of mSOD1/Srf KO mice was significantly higher than in mSOD1 mice in most timepoints after 8 weeks. Female mSOD1/Srf KO animals also displayed an earlier appearance of symptoms (NeuroScore 1), but the magnitude was smaller (Figure 2D).

We employed grip measurement (Figure 2E, F) and the inverted grid test (Figure 3A, B) to assess grip strength. In mSOD1 mice of both sexes, grip strength began to diverge from WT and SRF KO mice at the age of 7-8 weeks (1, 6). Loss of SRF in MNs of the mSOD1/Srf KO cohort resulted in a more pronounced decrease in grip strength, which was evident at the age of 8 weeks. However, by the age of 15 weeks, the male mSOD1/Srf KO mice were no longer different from male mSOD1 mice (Figure 2E). A similar trend was observed for females, although the lower sample numbers precluded a higher statistical significance (Figure 2F).

In the inverted grid test (Figure 3A, B), male and female mSOD1 mice were no longer able to complete the test by the age of 8 weeks (falling down before 180s). At the same age mSOD1/Srf KO mice displayed shorter holding times than mSOD1 animals (Figure 3A, B) indicating a more severe motor impairment in alignment with the grip strength results (Figure 2E, F). In contrast, WT and Srf KO mice adhered to the grid for $\geq$180 seconds over the entire 16-week period.

Moreover, we assessed mice for motor coordination in the pole climb-down test (Figure 3C, D). Here, most of the mSOD1 mice were no longer able to climb down the pole at the age of 13 weeks. mSOD1/Srf KO mice were unable to climb down the pole at a significantly earlier age, and when capable, required a significantly longer time than mSOD1 mice. WT and Srf KO mice were consistently able to complete the task.

Finally, we characterized the disease onset based on the body-weight curves (Figure 2A, B), determining the presymptomatic (onset) phase and the progression phase durations (38). SRF ablation in males (Figure 3G) but not in females (Figure 3H) resulted in a significantly earlier onset of disease, although the duration of the progression phase remained unaffected. Surprisingly, despite the earlier onset of symptoms, no difference was found between mSOD1 and mSOD1/Srf KO mice (either male or female) in relation to their survival (Figure 3E, F).

Taken together, loss of SRF in MNs causes an earlier disease onset and a more profound initial motor impairment in male and – to some extent – female mice. Surprisingly, this finding did not align with a shorter survival, indicating that SRF plays a role in determining the vulnerability of a subset of MNs that are affected first (the FF-MN).

SRF deletion in MNs enhances microglial reactivity and denervation of neuromuscular junctions

Next, we investigated the histopathological basis of the earlier and more severe disease onset in mSOD1/Srf KO mice (Figure 4). More specifically, we assessed microgliosis and astrogliosis in the ventral horn of the lumbar spinal cord (Figure 4A-D). WT and Srf KO mice were comparable in astrocyte and microglia density (Figure 4A, B). mSOD1 mice exhibited marked astrogliosis and microgliosis, which was significant at P50 and further intensified at

P90 (Figure 4C; M, N). Notably, at P50 – but not P90 – mSOD1/Srf KO mice displayed a higher degree of microgliosis compared to mSOD1 littermates and a tendency for higher astrogliosis (Figure 4D; M, N). This was corroborated by an additional marker CD68, indicating microglia-associated phagocytosis (Supp. Figure 4). Overall, there was a slight increase in microgliosis and astrogliosis at P50 but not P90 when SRF was deleted in mSOD1 mice.

Furthermore, quantification of MNs (Figure 4O) revealed reduced MN numbers in mSOD1 (Figure 4G) and mSOD1/Srf KO (Figure 4H) mice compared to WT (Figure 4E) and Srf KO (Figure 4F). However, no differences between mSOD1 and mSOD1/Srf KO were discernible (Figure 4O).

Finally, we scrutinized the extent of neuro-muscular junction (NMJ) denervation (Figure 4I-L; P). SRF loss appears to primarily affect the early disease phase, when FF-MN denervate and, subsequently, degenerate. Thus, we focused on the L1 subcompartment of the *lateral gastrocnemius*, containing only FF motor units denervating at about P55 (1, 6, 18). To label the presynaptic terminals and the axons, muscle sections were immunostained for synaptophysin and ßIII tubulin, respectively. Thereafter, sections were stained with fluorescently-labelled bungarotoxin (BTX) to identify the post-synaptic NMJ plaques (Figure 4I-L). NMJs were considered "innervated" if the overlap between the pre- and post-synaptic markers was >70% of the NMJ area. In this respect, both WT and SRF KO mice displayed >80% fully innervated NMJs. mSOD1 mice displayed a trend towards a decrease in L1 innervation (Figure 4P). However, by P50, the mSOD1/Srf KO mice exhibited a significant degree of NMJ denervation, once again indicating an earlier disease onset (arrows Figure 4L; P). At P90, mSOD1/Srf KO animals still displayed a trend towards more severe denervation than in mSOD1 mice (Figure 4L; P).

Thus, disease markers show an earlier and mildly enhanced microgliosis and NMJ denervation in mSOD1/Srf KO mice.

Reduced autophagy induction and enhanced misfolded SOD1 accumulation upon SRF deletion in SOD1^{G93A} mice

Autophagy induction is one of the cellular hallmarks described in several ALS mouse models, including SOD1^{G93A} mice (19, 37, 41) and human MNs (42). Furthermore, autophagy impairment has previously been hypothesized to be mechanistically related to MN vulnerability (43).

Therefore, we analyzed whether SRF loss affects the autophagic pathway in MNs of the mSOD1 model (Figure 5). At P50, lumbar spinal cord sections were obtained from male mice representing the four genotypes (Figs. 2-4) and were immunostained for the early autophagy marker Beclin-1 (Figure 5A-D; U), the autophagy substrate p62 (Figure 5E-H; V) as well as for the lysosomal marker Lamp1 (Figure 5I-L; W).

Compared to WT or Srf KO littermates, mSOD1 mice displayed MNs with an increased burden of Beclin-1 positive structures located in the cell body (see arrows Figure 5C). Surprisingly, in mSOD1/Srf KO mice, very few MNs displayed high levels of Beclin-1^{+} aggregates and Beclin-1 intensity in MNs was significantly lower than in mSOD1 mice (Figure 5D; U). Similarly, a MN subset in mSOD1 mice displayed round inclusions that were brightly immunopositive for p62 (37, 41). Once again, in mSOD1/Srf KO mice, MNs displaying p62 inclusions were rare and had smaller p62 inclusions (Figure 5H, V). In fact, most MNs in mSOD1/Srf KO were devoid of p62 inclusions (Figure 5H, V). In line with the apparent decrease in the activity of the autophagic pathway following SRF loss, we found that the Lamp1 was not upregulated in

mSOD1/Srf KO mice (Figure 5L, W) when compared to mSOD1 mice (arrows in Figure 5K). We also inspected LC3, a marker of the terminal stages of autophagy flux (Supp. Figure 5). On a protein level, LC3 abundance was enhanced in mSOD1/Srf KO mice compared to mSOD1 mice (Supp. Figure 5). Above we noted that lysosomal abundance analyzed by Lamp1 was decreased in mSOD1/Srf KO mice (Figure 5L, W). Thus, fusion of LC3 positive autophagosomes with lysosomes in the final stages of autophagic flux might be impaired by SRF deletion, thereby resulting in the accumulation of LC3 positive autophagosomes in mSOD1/Srf KO mice.

Since SRF ablation appeared to interfere with autophagy-mediated protein degradation, the abundance of misfolded SOD1 was monitored (Figure 5Q-T; X). Interestingly, in line with reduced autophagy, the misfolded SOD1 burden (Figure 5S) was significantly elevated in mSOD1/Srf KO (Figure 5T) compared to mSOD1 (Figure 5S) mice at P50 (quantified in Figure 5X).

Taken together, SRF loss interferes with the activity of the autophagic pathway, and this observation correlated with a heavier burden of misfolded SOD1 in SRF deficient MNs.

SRF ablation reduces autophagy gene mRNA abundance in mutant SOD1 MNs

So far, SRF has not been revealed as a transcription factor associated with autophagy in any cell type. However, given the impact of SRF loss on MN autophagy (Figure 5), we questioned whether SRF could affect transcription of genes encoding for the autophagy pathway (Figure 6). Thus, we micro-dissected individual MNs for mRNA extraction and cDNA synthesis in the lumbar ventral motor column in P50 male mice of the four genotypes (see scheme Figure 6). qPCR analysis confirmed comparable human *SOD1* transgene expression in the mSOD1 and

mSOD1/Srf KO cohort with no *SOD1* mRNA detected in WT and Srf KO mice (Figure 6A). *Srf* mRNA deletion was validated in Srf KO and mSOD1/Srf KO mice (Figure 6B). Furthermore, several IEGs known as SRF targets (25, 36) such as *cFos* (Figure 6C), *Egr1* (Figure 6D) or *Npas4* (Figure 6E) were reduced in Srf KO and – to a similar extent – in mSOD1/Srf KO mice, thus providing confirmation of an impairment in SRF-dependent transcription.

A first gene set including *Atg101, Atg9a, Atg10* and *Atg14* (Figure 6F-I) was downregulated in Srf KO MNs. Albeit to a lesser extent, these genes were also downregulated in mSOD1 MNs in comparison to the WT. Of particular significance, these genes were even further decreased in mSOD1/Srf KO MNs compared to mSOD1 MNs (Figure 6F-I). A second gene set encompassing *Map1lc3a (i.e., Lc3a), Beclin1* and *Atg7* (Figure 6J-L) showed a substantial mRNA upregulation indicative of autophagy induction in mSOD1 samples, however, their expression was downregulated in Srf KO mice and abrogated in mSOD1/Srf KO MNs. This data indicates impaired autophagy induction upon SRF deletion due to reduced mRNA levels of autophagy genes. We also analyzed p62, a gene that has previously been investigated on the protein level (Figure 5). Here, p62 levels were upregulated in SRF deficient MNs and mSOD1/Srf KO MNs, suggesting a SRF repressor function in WT MNs (Figure 6M). *Lamp5* was downregulated in Srf KO, mSOD1 and mSOD1/Srf KO MNs in comparison to WT (Figure 6N). Two further autophagy encoding genes, *Ulk1* and *Fip200*, were not obviously affected (Figure 6O, P). To assess direct SRF promoter occupancy, chromatin immunoprecipitation (ChIP) was performed (Supp. Figure 6). *Atg7, Atg9a* and *Atg10* were predicted to contain SRF binding sites (CArG boxes; see Supp. Table 2) and enhanced SRF promoter occupancy for those genes was observed (Supp. Figure 6).

In summary, SRF loss affects transcriptional regulation of multiple autophagy genes and autophagy induction in ALS MNs requires SRF.

SRF-VP16 reduces neurodegeneration associated induction of autophagic genes

Previously, we noted decreased induction of autophagy related proteins (Figure 5) and mRNA abundance (Figure 6) upon SRF loss-of-function. To corroborate SRF's transcriptional regulation on autophagy encoding genes, we performed gain-of-function experiments with SRF-VP16, a constitutively-active SRF protein (44). As a control, SRF-VP16ΔMADS was used which did not contain the MADS box, thereby precluding DNA binding (44). Considering that the accumulation of misfolded-proteins induces autophagy, we further asked whether SRF-VP16 reduces misfolded-protein abundance triggered by autophagy induction. For this purpose, neurodegeneration-associated autophagy was induced by Poly-GA aggregates recapitulating C9orf72-associated ALS pathological features (20).

An equal abundance of SRF-VP16 or SRF-VP16ΔMADS mRNA (Figure 7A) and GFP-tagged Poly-GA aggregates was documented by qPCR (Figure 7B). As expected, SRF-VP16 – but not SRF-VP16ΔMADS – induced the SRF target gene *cFos* (Figure 7C).

In total, we tested eight autophagy encoding (Figure 7D-K) and one lysosomal pathway encoding gene (*Lamp5*; Figure 7L). SRF-VP16, but not SRF-VP16ΔMADS, induced four out of the eight autophagy encoding genes, including *Atg9a* (E), *Atg10* (F), *Beclin1* (I) and *Atg7* (J) as well as *Lamp5* (L). Moreover, all genes upregulated by Poly-GA expression, *Atg9a* (E), *Atg10* (F), *Atg14* (G), *Beclin1* (I), *Atg7* (J) and *Lamp5* (L) were down-regulated by SRF-VP16. This suggests that SRF-VP16 exerts transcriptional activation under typical physiological cell conditions, whereas SRF-VP16 acts as transcriptional repressor in the context of a

neurodegenerative inducing protein. Conversely, in the presence of SRF-VP16ΔMADS, Poly-GA aggregate-mediated transcriptional induction persisted. Other genes, including *Atg101* (Figure 7F), *Map1lc3a* (Figure 7H) and *p62* (Figure 7L), were not obviously modulated by either SRF-VP16 or Poly-GA expression.

Besides SRF-VP16, we additionally analyzed whether MRTF-A, an SRF cofactor with considerable neuronal functions, (20) also mediates transcriptional regulation of autophagy genes in the context of Poly-GA inflicted aggregate formation (Supp. Figure 7). MRTF-A was also found to be upregulated the same set of autophagy and lysosome encoding genes (Supp. Figure 7). Furthermore, Poly-GA mediated induction of the aforementioned genes was also counteracted by MRTF-A (Supp. Figure 7). Besides Poly-GA, we analyzed whether SRF-VP16 can reduce autophagy encoding genes induced by mutant SOD1 proteins, resulting in aggregate formation ($SOD1^{G93A}$ and $SOD1^{A4V}$; (45)**.** SRF-VP16 reduced the mRNA abundance of *Atg9a, Atg10, Atg7* and *Lamp5* which were induced by both $SOD1^{G93A}$ and $SOD1^{A4V}$ (Supp. Figure 8).

In summary, SRF-VP16 can dampen autophagy induction prompted by an established ALS associated protein aggregate.

SRF-VP16 modulates autophagy and reduces ALS-associated aggregate formation

The aforementioned data suggests that SRF-VP16 induces autophagy encoding genes in healthy cells, depicting SRF's potential to regulate their gene transcription (Figure 7). Upon ALS-associated aggregate formation, however, SRF-VP16 had the reverse function and down-regulated mRNA abundance of several autophagic genes induced by aggregates (Figure 7). Thus, SRF-VP16 could potentially serve as a novel tool to modulate autophagy and aggregate clearance in neurodegeneration. This potential SRF-VP16 function was analyzed by live

recording of autophagy, Poly-GA aggregate clearance and lysosomal co-localization (Figure 8).

Here, cells were transfected with a p62-GFP-mCherry construct which indicates an enhanced autophagic flux by a green to red fluorescence switch (46). SRF-VP16 (Figure 8C, D; Supp. Video 2) but not as much SRF-VP16ΔMADS positive cells (Figure 8A, B; Supp Video 1) notably lowered the GFP:mCherry ratio (Figure 8I). This indicated more p62 presence in autophagy vesicles upon SRF-VP16 expression. Furthermore, the area of C9orf72 derived Poly-GA aggregates was measured (Figure 8E-H). Here, SRF-VP16 (Figure 8G, H; Supp. Video 4) reduced the aggregate size compared to SRF-VP16ΔMADS (Figure 8E, F; Supp. Video 3) expressing cells (quantified in Figure 8J). Finally, the co-localization of aggregates with lysosomes was measured to estimate a potential clearance of Poly-GA aggregates in lysosomes (Figure 8E-H; K). In SRF-VP16 positive cells, a more significant overlap of Poly-GA aggregates and lysosome signals (yellow in Figure 8G, H) was observed compared to SRF-VP16ΔMADS (Figure 8E, F). Overall, the Poly-GA: lysosome ratio was 0.8 for SRF-VP16 and approximately 0.3 for SRF-VP16ΔMADS, suggesting more Poly-GA clearance in lysosomes by SRF-VP16 (Figure 8K).

In summary, cell culture showed enhanced autophagic aggregate clearance by SRF-VP16.

Neuronal activity modulates ALS-associated autophagy and disease burden through SRF

Previous chemogenetic studies have demonstrated that increased neuronal excitability promotes neuroprotection in MNs by reducing the accumulation of misfolded SOD1. Conversely, decreasing MN excitability exacerbates the disease burden (18). To date, no TF

has been identified to connect neuronal activity with such neuroprotective cellular processes, including reduction of misfolded SOD1 abundance and autophagy.

In the next step we asked whether SRF could provide a transcriptional link between neuronal excitability and neuroprotective programs. For this, we employed PSAM/PSEM chemogenetics (47) in mSOD1/SRF wt and mSOD1/Srf KO mice. We hypothesized that chemogenetic modulation of neuronal excitability in diseased MNs should fail in the absence of SRF (Figure 9). To address this, the pharmacologically selective actuator module (PSAM) coupled either to 5HT3-receptor (PSAM-Act; positive MNs labelled with BTX in red) for neuronal depolarization or to a glycine-receptor (PSAM-Inh; positive MNs labelled with GFP in green) for neuronal hyperpolarization was overexpressed in MNs (see Figure 9A). In all three conditions (ctr, PSAM-Act and PSAM-Inh) the expression levels of SRF in MNs was comparable (Supp. Figure 9).

In line with previous reports in mSOD1 mice (18), enhanced neuronal activity (act. PSAM; Figure 9C) decreased, whereas lowering neuronal activity through inhibitory PSAM (Figure 9D) enhanced the misfolded SOD1 burden in MNs (Figure 9N) compared to the control (no AAV9 infection; Figure 9B). Besides misfolded SOD1 accumulation, autophagy was assessed through quantification of LC3A abundance in mSOD1 mice (Figure 9H-J; O). In alignment with previous reports (19, 48), here we showed that act. PSAM (Figure 9I) decreases, whereas inh. PSAM (Figure 9J) increases the autophagic response in ALS diseased MNs (Fig 9O).

In the next step, chemogenetics was also performed in mSOD1/Srf KO mice (Figure 9E-G; K-M). In contrast to the mSOD1 mice with wildtype SRF, chemogenetic mediated elevation of neuronal excitability with act. PSAM failed to lower the misfolded SOD1 level in MNs (Figure 9F) compared to control (Figure 9E; see N). Likewise, inh. PSAM overexpression did not alter misf. SOD1 levels compared to control (Figure 9K, M; N). As seen in misf. SOD1, levels of

LC3A were not altered in mSOD1 mice as a result of chemogenetic manipulation in the absence of SRF (Figure 9K-M; O).

This indicates that neuronal excitability engages SRF to exert neuroprotective processes in ALS diseased MNs.

Discussion

In the present study, we demonstrated that a prototypical activity-dependent TF, SRF, is required for the upregulation of autophagy genes in response to misfolded SOD1 accumulation in $SOD1^{G93A}$ mice. MN-selective SRF deletion caused an earlier disease onset (Figs. 2 and 3). Surprisingly, the effect of SRF deletion progressively disappeared. At around P90, no difference was observed in relation to performance, survival and disease marker burden (Figs. 2-4). Furthermore, female mSOD1/Srf KO mice showed less severe phenotypes compared to males, which is in line with previous reports (39). Overall, this suggests that SRF is critical for reducing FF-MN vulnerability at an early stage of disease progression (around P50-P60), but likely not for other MN subpopulations (see summary Figure 10A). Additionally, this difference in early vs. late SRF involvement might also correlate with an early hyperexcitabilty vs. a later hypoexcitability of MNs during disease progression (see below). Importantly, SRF constitutes the first molecular link between neuronal activity and proteostatic autophagy responses in MNs, suggesting that the former may contribute to MN vulnerability by controlling the latter.

SRF, together with CREB, is a major TF in response to synaptic activity (23, 24). In fact, SRF-mediated transcriptional activation is a signature of physiological and pathophysiological states associated with increased synaptic input and neuronal activity. For propagation of physiological neuronal activity, SRF has been linked to the long-term remodeling of neuronal structure and function upon experience: loss of SRF interferes with the induction of both long-term potentiation (28) and long-term depression (27, 49). Similarly, in pathology, neuronal activity elicited by traumatic brain injury (36), Alzheimer's disease (50, 51) and epilepsy (25, 26) are targeting SRF. So far, SRF has mainly been associated with neuroprotective functions including axonal growth in development (52-55) and neuronal injury (32, 33, 36). The

premature disease onset upon SRF loss in the SOD1 mouse ALS model is also congruent with such a neuroprotective SRF function in spinal MN neurodegeneration. In fact, SRF appears necessary to sustain FF-MNs, suggesting that FF-MNs may be more dependent on activity-regulated transcriptional programs. In agreement with this premise, SRF was strongly present in FF-MN (Figure 1) and a decrease in SRF+ neurons can be elucidated in terms of their high vulnerability to disruption of synaptic inputs and excitation.

Until now, one of SRF's main transcriptional outputs is IEG regulation including Fos and Egr family members, ATF3 and Npas4. Together with SRF, these downstream TFs may potentially propagate a further neuronal gene expression wave, thereby granting SRF a widespread footprint on the neuronal transcriptome. Interestingly, overexpression of the SRF transcriptional target ATF3 improves motor function in $SOD1^{G93A}$ mice (56).

Herein, we observed an SRF role in transcriptional regulation of cellular proteostasis which was previously unappreciated. The expression of eight autophagy encoding genes was affected by SRF deletion in mSOD1 mice (Figure 6). This resulted in an overall lower protein level (Figure 5) and mRNA abundance (Figure 6) of autophagic genes in SRF deficient MNs. Conversely, SRF gain-of-function enhanced mRNA abundance of several autophagy encoding genes and elevated autophagy, Poly-GA aggregate removal and lysosomal degradation on the cellular level (Figs. 7 and 8).

Overall, SRF gain- and loss-of-function suggest a novel SRF role in the modulation of ALS associated autophagy and proteostasis. In vulnerable MNs, such an impaired autophagy induction might contribute to the earlier disease onset observed upon SRF deletion (Figure 10). Thus, in WT mice, functional SRF provides a neuroprotective function to SOD1 affected MNs. In diseased MNs, SRF ensures a certain extent of autophagy and lysosomal dependent aggregate clearance, thereby providing some neuroprotection to MNs (Figure 10B). Once SRF

is depleted, autophagy and lysosomal degeneration is reduced and worsens MN pathology (Figure 10C). In alignment with this, we demonstrated that SRF-VP16 can decrease disease burden (Figure 8). Here, a C9orf72 dependent ALS assay was used in addition to the SOD1 mouse model, allowing for the analysis of c9orf72 derived protein aggregates. Thus, SRF activity affected neurodegeneration in two different ALS associated mutant proteins, suggesting that SRF's neuroprotective function is not limited to single ALS experimental models.

Bioinformatic analysis and ChIP revealed direct SRF binding sites in the promoter of five out of 18 autophagy genes (Supp. Table 2, Supp. Figure 6). This suggests that SRF may directly regulate some autophagy encoding genes. However, this also implies that other TFs such as CREB (57) or SRF directed IEGs known to regulate autophagy (58, 59) might provide a link between neuronal activity and autophagy gene regulation. So far, only two instances of an SRF connection with autophagy have been reported (60, 61). Here, SRF protected from rotenone-induced cellular death and reduced synuclein aggregation, however, this beneficial effect was abolished by either *Beclin1* or *Atg5* knock-down, implying that autophagy induction is a critical component of the neuroprotective SRF effects (60). This cell culture finding supports our conclusion that in response to neuronal activity, SRF modulates autophagy to convey neuroprotection. Finally, SRF was shown to be subject to autophagy-dependent degradation (61). This points at a reciprocal regulatory mechanism whereby SRF might regulate mRNA abundance of autophagy encoding genes. In turn, this may potentially have a negative feed-back on SRF abundance on the protein level.

As discussed above, SRF transcriptional regulation on autophagy encoding genes appears as one mechanism by which SRF modulates disease progression in the SOD1 mouse model. However, given SRF's wide impact on regulating a wealth of different target genes including

IEGs and actin cytoskeletal genes (23) those SRF regulated gene classes might additionally contribute to the observed phenotypes.

In ALS pathogenesis, disruption of autophagic degradation of misfolded proteins is suggested to be a critical event (41-43, 62-64). Interestingly, 60% of vulnerable MMP9 positive MNs were strongly positive for SRF (FF-MN; Figure 1). Thus, SRF loss might disproportionately affect this subpopulation, suggesting that sustaining a sufficient level of autophagy in FF-MNs may be an important protective mechanism, and that activity-dependent transcriptional programs mediated by SRF may be involved in the autophagic response in FF-MN. It is worth noting that in sporadic human ALS cases (Supp. Table 1), MNs contained SRF structures reflecting nuclear rods (Supp. Figure 1). These were not seen in mouse MNs which may be due to the specific $SOD1^{G93A}$ mutation not producing these alterations. Although speculative, such rod-like nuclear structures in human MNs are reminiscent of cytoskeletal proteins (e.g., cofilin) which occur in nuclear rods of other neurodegenerative diseases (65, 66).

Is neuronal activity of FF-MNs necessary to uphold the autophagic pathway through SRF? The role of excitation and synaptic integrity in determining MN vulnerability in ALS is currently controversial. According to the excitotoxicity hypothesis, high levels of glutamatergic excitatory inputs – alone, or together with increased intrinsic excitability of MNs – would be sufficient to drive MN cell death (67, 68). However, recent work has suggested that rather than being hyperexcitable, MNs display an early increased excitability followed by hypoexcitability in vulnerable MNs later on (3, 13, 15, 69). This dynamic shift has also been observed in iPSC-derived MNs (17, 20, 70). Moreover, impaired synaptic function and reduced synapse numbers were shown in SOD1 mice and iPSC-derived MNs (19, 20, 71, 72). Thus, it is conceivable that the appearance of hypoexcitability and synapse loss may precipitate neuronal death by reducing

SRF activation and terminally imbalancing the autophagic pathway. As previously demonstrated by chemogenetic control of MN firing (18, 19), one may predict that sustaining some degree of excitability may actually be beneficial. This prediction is corroborated in this study by showing that enhanced MN excitability not only lowers misf. SOD1 levels (18) but also autophagy marker abundance (Figure 9). So far, no molecular mechanism has been identified as a target for neuronal activity's neuroprotective impact on MNs. By combining the genetic deletion of SRF with chemogenetics in mice, this study revealed that SRF is required for neuronal activity to modulate disease progression (Figure 9). This provides a molecular framework to interpret the activity-dependent neuroprotection in ALS, but possibly other neurodegenerative conditions as well (8).

In conclusion, this study provides a mechanistic link between neuronal activity, synaptic inputs and autophagy imbalance (Figure 10). In doing so, we shed further light on a previously unappreciated role of SRF as regulator of the neuronal proteostasis. These findings may have implications in other neurodegenerative conditions characterized by protein aggregates (such as Parkinson disease and Huntington disease) in which loss of neuronal firing appears to be the watershed event leading to the demise of vulnerable neuronal populations (8).

Materials and methods

Transgenic mice breeding strategy and housing

In order to get triple-transgenic *hSOD1*^{G93A}/*ChAT*^{Cre}/*Srf*$^{loxp/loxp}$ animals, *ChAT*^{Cre} mice (Jax strain number: 006410) were first crossed with *Srf* floxed mice (52, 73). It is worth noting that *ChAT*^{Cre} mice allowed for the deletion of cholinergic cells such as MNs, but also other cell types including skin cells (74). This mouse double transgenic line (*ChAT*^{Cre}/*Srf*$^{loxp/loxp}$) was further crossed to high-copy hSOD1^{G93A} mice (Jax strain number: 002298) to get *hSOD1*^{G93A}/*ChAT*^{Cre}/*Srf*$^{loxp/loxp}$ triple transgenic mice. This allowed for the motor neuron-specific *Srf* knock out in an ALS mouse model. This triple transgenic mouse line was maintained by mating *hSOD1*^{G93A}/*ChAT*^{Cre}/*Srf*$^{loxp/wt}$ males to *hSOD1*$^{-}$/*ChAT*^{Cre}/*Srf*$^{loxp/wt}$ females. From these breedings, four groups were derived: 1.) WT (*hSOD1*$^{-}$/*ChAT*$^{Cre/}$*Srf*$^{wt/wt}$), 2.) mSOD1 (*hSOD1*^{G93A}/*ChAT*^{Cre}/*Srf*$^{wt/wt}$); 3.) Srf KO (*hSOD1*$^{-}$/*ChAT*^{Cre}/*Srf*$^{loxp/loxp}$), 4.) mSOD1/Srf KO (*hSOD1*^{G93A}/*ChAT*^{Cre}/*Srf*$^{loxp/loxp}$).

Mice were kept with free access to food and water in a pathogen-free animal facility at the University of Ulm, with a 12h day-night shift, and appropriate temperature and humidity conditions. Humane endpoints of mSOD1 and mSOD1/Srf KO mice were determined individually according to the criteria indicated below.

Behavior Tests and Survival Analysis

Mice were genotyped 21 days postnatally (P), then introduced blindly to a researcher. Behavior tests in the exploration and the in-depth cohort were carried out by different researchers during a similar day period (early afternoon). The researcher was introduced to the mice by handling and training at three weeks to reduce stress. From four until 20 weeks, all tests were carried out

in the following order based on the stress level of the tests. In the pole test and inverted grid test, housing materials were applied at the bottom of the cage to prevent any possibility of injury from falling.

1.) Body-weight

Body-weight was measured twice a week, always before the other behavior tests. With a 0.1g accuracy balance, the average of three measurements were recorded.

2.) Neurological score (NS)

Neurological score (37, 38, 40) was determined twice a week by tail suspension test, 25 cm walking test and righting reflex. Briefly, holding two seconds for completely spreading of hindlimbs was considered NS=0; partially collapsing and a normal gait were considered NS=1; partially collapsing, slower walking with no more than two toe mistakes were considered NS=2; total collapsing or more than two toe mistakes, but a righting reflex less than 10 seconds were considered NS=3; and at least one hindlimb paralysis or righting reflex over 10 seconds were considered NS=4.

3.) Pole test

Pole tests were carried out once a week. Mice were put head up on the top of a vertical pole (rough wood, 50 cm high, Ø 1cm). In healthy conditions, mice would make a turn and walk along the pole to reach the cage bottom. In disease conditions, mice would be slower, fail to turn, slide down the pole or even fall from the pole. The time between starting to turn and reaching the bottom was regarded as the time to finish, while 2 minutes were recorded if mice failed or fell. Five tries were performed per mouse and the best performance was recorded.

4.) Inverted grid test

The inverted grid test was performed once a week during which a mouse was suspended from an inverted grid (barbed wire, 1cm in between) to see how long it could hold itself. For a total of 3 minutes, the mice were given three tries and the longest time was recorded (max. 3 minutes).

5.) Grip strength

Forelimbs and fore-hind limbs grip strength were measured twice a week using a grip strength meter at maximum strength mode (Panlab, Harvard Apparatus). The highest value within 3 tries was recorded.

6.) Determination of survival and disease onset

Health conditions, motor ability and righting reflex were checked every day after mice reached NS=3; meanwhile, water and wet food were provided on the cage bottom. A loss of 30% of the peak body-weight or neurological score reaching 4 was considered a humane endpoint, while WT and Srf KO mice were sacrificed at P200. After the endpoint, the individual body-weight trend line was drawn and disease onset was determined depending on the peak body-weight age (38).

Intraspinal injections of AAV

The following AAV vectors were intraspinally injected: pAAV(9)-pCAG-A7-floxed-PSAM(L141F, Y115F)5HT3-WPRE and PSAM-Inhibitor pAAV(9)-pCAG-A7-floxed-PSAM(L141F, Y115F)-GlyR-GFP-WPRE. Intraspinal injection of AAV was performed as previously reported (18). Briefly, mice at day P26 were administered Buprenorphine (0.05 mg/kg; Reckitt Benckiser healthcare Ltd, Berkshire, UK) and Meloxicam (1.0 mg/kg; Metacam, Boehringer-Ingelheim, Ridgeland, CT) 30 min before isoflurane anesthesia (4% in O_2 at 800 ml/min). Dorsal laminectomy was performed at T11-T13 level and the posterior median vein was used as reference to inject two sites. A pulled glass capillary coupled to a Picospritzer III apparatus was used to inject 0.5 μl AAV mixed with 0.5 μl 1.5% Fast-green (coordinates y = +0.25 mm z = –0.4 mm). Different AAVs were injected 2 mm away (longitudinally), with both order and position being randomized. Once completed, muscles and skin were stitched with Prolene 7.0 surgical threads and animals were transferred to single cages with facilitated access to food and water. Mice were monitored for 72 h and were administered buprenorphine twice/day and meloxicam once/day. The PSEM308 effector molecule was administered from 7 days after surgery for 8 consecutive days at a dose of 5 mg/kg in saline. Mice were sacrificed 3h after the last agonist administration.

Histology and immunofluorescence

Mice were anesthetized with 5 mg/kg ketamine and 5 mg/kg xylazine by intraperitoneal injection and perfused with ice-cold PBS (2 ml/g), followed by 4% PFA in PBS (2.5 ml/g). Spinal cords lumbar enlargements were harvested and further fixed in 4% PFA in PBS at 4°C overnight, cryopreserved in 30% sucrose in PBS until sinking, embedded in OCT (TissueTek) and cross-sectioned on cryostat microtome at 40 µm (Leica 1900s). Free-floating fluorescence staining was performed as previously reported (37). In brief, spinal cord sections were blocked

with 3% BSA and 0.3% Triton in PBS 2h then followed by 1st antibodies (see antibody list in Supplement) in blocking solution on a shaker at 4°C for 48h. After washing (PBS, 3 x 30 min), 2nd antibodies (see supplement) were incubated at RT for 2h. Samples went through washing steps before being mounted with ProLong Gold Antifade Reagent (Invitrogen). Similar procedures were performed for neuromuscular innervation analysis; however, gastrocnemius muscles were post-fixed in 4% PFA for 2h and sectioned longitudinally at 30 μm; and muscle samples were blocked with 6% BSA, 10% Donkey Serum and 0.9% Triton in PBS.

Confocal image acquisition and data analysis

All fluorescence images were acquired with LSM-710 confocal microscopy (Carl Zeiss) or Leica DMi8 inverted microscope. Images were captured in 8-bit format at a 1024x1024 resolution and an optimal optical section thickness (z). Multi-channel acquisitions were set up independently according to the excitation and emission spectra to get saturated and cross-talk free images. A z-stack with individual sections 1 μm apart was scanned continuously. Spinal cord images were acquired at the ventral horn. Gastrocnemius samples were acquired at L1 branch (1). All pictures were processed with ImageJ (FIJI) and a maximum intensity z-projection was performed. MN cell bodies were traced manually with a freehand selection tool recognized by VAChT or ChAT, followed by measurement of grey values of individual MNs. A threshold was set to avoid the background signal if a positive area was measured. MN numbers were counted in the original z-stack sequence. In the same staining, MNs from at least five ventral horns per mouse were analyzed. The NMJ innervation analysis was performed using the colocalization plugin and over 70% overlapping area of pre- and post-synapse was considered innervated. At least 100 L1-branch gastrocnemius NMJs per mouse were measured.

645

Cell culture

HEK293 cells (from Leibniz-Institut DSMZ, Germany) were transfected with polyethyleneimine and 2 μg of plasmid DNA in serum-free medium. After 5 hours, complete medium was added. Cells were transfected with the following constructs: GFP (as control), SRF-VP16, SRF-VP16 ΔMADS (44), constitutively-active MRTF-A (52), Poly-GA (75), $SOD1^{G93A}$ (47), $SOD1^{A4V}$ (45) or P62-GFP-mCherry (46). For the Poly-GA-lysotracker experiment, after overnight incubation, 1 μM Lysotracker Deep Red (Thermo Fisher) was added and incubated for 2 hours at 37°C. For qPCR experiments with HEK293 cells, RNA was extracted with TRIzol (Qiagen). For reverse transcription, 1 μg RNA was mixed with random primers dN6 (Biomers), incubated for 10 minutes at 70°C and placed on ice. Then, the master mix (RT 5x buffer, Promega Biosciences), dNTPs (Genaxxon), Ribolock RNase Inhibitor (Thermo Scientific), M-MLV RT RNase (Promega Biosciences) were added. After 10 minutes at room temperature, the mixture was incubated at 42°C for 45 minutes, at 99°C for 3 minutes and, thereafter, on ice.

qPCR

qPCR was performed by mixing 2 μl cDNA, specific primer pairs and SYBR Premix Ex Taq (Tli RNase H Plus) PCR Master Mix (TaKaRa Bio Europe, Saint-Germain-en-Laye, France) in a total volume of 10 μL per well. The following settings were used in the Light Cycler 480 (Roche): 2 min at 50°C and 10 min at 95°C, followed by 50 cycles of PCR for 15 s at 95°C for denaturation and 1 minute at 60°C for annealing and elongation. The LC480 II software was used to detect the cycle threshold values. Relative mRNA expression of each target gene was

calculated relative to the house-keeping gene *Gapdh* (glycerinaldehyde-3-phosphate-dehydrogenase) with the ΔCt method. All experiments were performed in technical duplicates. Primer details are provided in the supplementary information.

Live cell imaging

All live cell imaging was performed on the Nanolive 3D Explorer (Nanolive, Switzerland). Cells were imaged at 60x magnification using the holotomography and fluorescence modalities. One frame was taken every 2 minutes for 1.5 hours. All frames were processed with ImageJ (FIJI) and a maximum intensity z-projection was performed. A threshold was set to avoid background signal followed by mean gray value and area measurements.

Statistics

All data were calculated in Excel (Microsoft Office 2019) and further compared in GraphPad Prism Software (v. 7.0). All values are expressed as mean ± SD unless otherwise indicated. The student t-test was applied to compare mean values in two groups. One-way ANOVA was applied for single time point markers among multiple groups. Paired two-way ANOVA with Tukey correction was carried out to compare the multi-time point markers and behavior test results. Survival and onset analysis were performed using the Mantel-Cox statistical test. Significance was assessed: *P<0.05, **P<0.01, *** P<0.001.

Study approval

All animal experiments followed the institutional guidelines of the local animal facility (Tierforschungszentrum, Ulm University) and EU laws. Animal experiments were approved by the Regierungspräsidium Tübingen (Tübingen, Germany). For human ALS samples, written informed consent was received prior to participation. The collection and the study were authorized by the ethics committee of Ulm University.

Data availability

Data are available from the corresponding author upon request.

Author contribution

JS and ND are shared first authors. JS is mentioned first since he started the project. BK and FR conceived the study and supervised the project. JS, ND, FR and BK planned the experiments. DS and JS performed the behavior experiments. JS and ND performed the histological experiments, the imaging and the image analysis. ND and JS performed the chemogenetic experiments. ND performed the cell culture, qPCR and live cell imaging. JS, ND, FR and BK prepared figures and drafted the manuscript. All authors read and approved the manuscript. The authors have declared that no conflict of interests exist.

Acknowledgements

The authors would like to thank Thomas Lenk, Simone Feldengut, Diana Wiesner and Florian olde Heuvel for the dedicated technical and administrative support. We thank Kelly del Tredici and Heiko Braak for their help with human ALS samples. This work was supported by the Deutsche Forschungsgemeinschaft (DFG, German Research Foundation) through the grant No. 443642953 to FR and BK. FR is also supported by the DFG through the individual grant No. 431995586 and 446067541 as well as in the context of SFB1149 (DFG No. 251293561). FR is also supported by the Thierry Latran Foundation (grants Trials and Hypmotals), the Radala Foundation, the BMBF (FKZ 01EW1705A) and the German Center for Neurodegenerative Diseases (DZNE)-Ulm. BK is funded by the DFG – Project-ID 251293561 – SFB 1149. BK is further funded through individual grants by the DFG (Project number: 406037611 and 441734479).

References

1. Pun S, et al. Selective vulnerability and pruning of phasic motoneuron axons in motoneuron disease alleviated by CNTF. *Nat Neurosci*. 2006;9(3):408-19.
2. Kaplan A, et al. Neuronal matrix metalloproteinase-9 is a determinant of selective neurodegeneration. *Neuron*. 2014;81(2):333-48.
3. Leroy F, et al. Early intrinsic hyperexcitability does not contribute to motoneuron degeneration in amyotrophic lateral sclerosis. *Elife*. 2014;3.
4. Sharma A, et al. ALS-associated mutant FUS induces selective motor neuron degeneration through toxic gain of function. *Nat Commun*. 2016;7:10465.
5. Manuel M, and Zytnicki D. Molecular and electrophysiological properties of mouse motoneuron and motor unit subtypes. *Curr Opin Physiol*. 2019;8:23-9.
6. Saxena S, et al. A role for motoneuron subtype-selective ER stress in disease manifestations of FALS mice. *Nat Neurosci*. 2009;12(5):627-36.
7. Blum JA, et al. Single-cell transcriptomic analysis of the adult mouse spinal cord reveals molecular diversity of autonomic and skeletal motor neurons. *Nat Neurosci*. 2021;24(4):572-83.
8. Roselli F, and Caroni P. From intrinsic firing properties to selective neuronal vulnerability in neurodegenerative diseases. *Neuron*. 2015;85(5):901-10.
9. Kuo JJ, et al. Increased persistent Na(+) current and its effect on excitability in motoneurones cultured from mutant SOD1 mice. *J Physiol*. 2005;563(Pt 3):843-54.
10. van Zundert B, et al. Neonatal neuronal circuitry shows hyperexcitable disturbance in a mouse model of the adult-onset neurodegenerative disease amyotrophic lateral sclerosis. *J Neurosci*. 2008;28(43):10864-74.
11. Pambo-Pambo A, et al. Early excitability changes in lumbar motoneurons of transgenic SOD1G85R and SOD1G(93A-Low) mice. *J Neurophysiol*. 2009;102(6):3627-42.
12. Bogaert E, et al. Amyotrophic lateral sclerosis and excitotoxicity: from pathological mechanism to therapeutic target. *CNS Neurol Disord Drug Targets*. 2010;9(3):297-304.
13. Martínez-Silva MdL, et al. Hypoexcitability precedes denervation in the large fast-contracting motor units in two unrelated mouse models of ALS. *Elife*. 2018;7.
14. Filipchuk A, et al. Early Hypoexcitability in a Subgroup of Spinal Motoneurons in Superoxide Dismutase 1 Transgenic Mice, a Model of Amyotrophic Lateral Sclerosis. *Neuroscience*. 2021;463:337-53.
15. Delestrée N, et al. Adult spinal motoneurones are not hyperexcitable in a mouse model of inherited amyotrophic lateral sclerosis. *J Physiol*. 2014;592(7):1687-703.
16. Devlin A-C, et al. Human iPSC-derived motoneurons harbouring TARDBP or C9ORF72 ALS mutations are dysfunctional despite maintaining viability. *Nat Commun*. 2015;6:5999.
17. Naujock M, et al. 4-Aminopyridine Induced Activity Rescues Hypoexcitable Motor Neurons from Amyotrophic Lateral Sclerosis Patient-Derived Induced Pluripotent Stem Cells. *Stem Cells*. 2016;34(6):1563-75.
18. Saxena S, et al. Neuroprotection through excitability and mTOR required in ALS motoneurons to delay disease and extend survival. *Neuron*. 2013;80(1):80-96.
19. Bączyk M, et al. Synaptic restoration by cAMP/PKA drives activity-dependent neuroprotection to motoneurons in ALS. *J Exp Med*. 2020;217(8).
20. Catanese A, et al. Synaptic disruption and CREB-regulated transcription are restored by K channel blockers in ALS. *EMBO Mol Med*. 2021;13(7):e13131.
21. Yap E-L, and Greenberg ME. Activity-Regulated Transcription: Bridging the Gap between Neural Activity and Behavior. *Neuron*. 2018;100(2):330-48.
22. Heinz DA, and Bloodgood BL. Mechanisms that communicate features of neuronal activity to the genome. *Curr Opin Neurobiol*. 2020;63:131-6.
23. Knoll B, and Nordheim A. Functional versatility of transcription factors in the nervous system: the SRF paradigm. *Trends in neurosciences*. 2009;32(8):432-42.

24. Benito E, and Barco A. The neuronal activity-driven transcriptome. *Molecular neurobiology*. 2015;51(3):1071-88.
25. Lösing P, et al. SRF modulates seizure occurrence, activity induced gene transcription and hippocampal circuit reorganization in the mouse pilocarpine epilepsy model. *Mol Brain*. 2017;10(1):30.
26. Kuzniewska B, et al. Adult Deletion of SRF Increases Epileptogenesis and Decreases Activity-Induced Gene Expression. *Molecular neurobiology*. 2016;53(3):1478-93.
27. Pulimood NS, et al. The Role of CREB, SRF, and MEF2 in Activity-Dependent Neuronal Plasticity in the Visual Cortex. *J Neurosci*. 2017;37(28):6628-37.
28. Ramanan N, et al. SRF mediates activity-induced gene expression and synaptic plasticity but not neuronal viability. *Nat Neurosci*. 2005;8(6):759-67.
29. Parkitna JR, et al. Loss of the serum response factor in the dopamine system leads to hyperactivity. *FASEB J*. 2010;24(7):2427-35.
30. Zimprich A, et al. Serum Response Factor (SRF) Ablation Interferes with Acute Stress-Associated Immediate and Long-Term Coping Mechanisms. *Molecular neurobiology*. 2017;54(10):8242-62.
31. Gerosa L, et al. SRF and SRFΔ5 Splicing Isoform Recruit Corepressor LSD1/KDM1A Modifying Structural Neuroplasticity and Environmental Stress Response. *Molecular neurobiology*. 2020;57(1):393-407.
32. Stern S, et al. Serum response factor modulates neuron survival during peripheral axon injury. *J Neuroinflammation*. 2012;9:78.
33. Stern S, et al. The transcription factor serum response factor stimulates axon regeneration through cytoplasmic localization and cofilin interaction. *J Neurosci*. 2013;33(48):18836-48.
34. Rieker C, et al. Ablation of serum response factor in dopaminergic neurons exacerbates susceptibility towards MPTP-induced oxidative stress. *Eur J Neurosci*. 2012;35(5):735-41.
35. Chang SH, et al. A novel role for serum response factor in neuronal survival. *J Neurosci*. 2004;24(9):2277-85.
36. Förstner P, and Knöll B. Interference of neuronal activity-mediated gene expression through serum response factor deletion enhances mortality and hyperactivity after traumatic brain injury. *FASEB J*. 2020;34(3):3855-73.
37. Ouali Alami N, et al. NF-κB activation in astrocytes drives a stage-specific beneficial neuroimmunological response in ALS. *EMBO J*. 2018;37(16).
38. Boillée S, et al. ALS: a disease of motor neurons and their nonneuronal neighbors. *Neuron*. 2006;52(1):39-59.
39. Pfohl SR, et al. Characterization of the Contribution of Genetic Background and Gender to Disease Progression in the SOD1 G93A Mouse Model of Amyotrophic Lateral Sclerosis: A Meta-Analysis. *J Neuromuscul Dis*. 2015;2(2):137-50.
40. Hatzipetros T, et al. A Quick Phenotypic Neurological Scoring System for Evaluating Disease Progression in the SOD1-G93A Mouse Model of ALS. *J Vis Exp*. 2015(104).
41. Rudnick ND, et al. Distinct roles for motor neuron autophagy early and late in the SOD1 mouse model of ALS. *Proc Natl Acad Sci U S A*. 2017;114(39):E8294-E303.
42. Catanese A, et al. Retinoic acid worsens ATG10-dependent autophagy impairment in TBK1-mutant hiPSC-derived motoneurons through SQSTM1/p62 accumulation. *Autophagy*. 2019;15(10):1719-37.
43. Chua JP, et al. Autophagy and ALS: mechanistic insights and therapeutic implications. *Autophagy*. 2021.
44. Schratt G, et al. Serum response factor is crucial for actin cytoskeletal organization and focal adhesion assembly in embryonic stem cells. *J Cell Biol*. 2002;156(4):737-50.
45. Turner BJ, et al. Impaired extracellular secretion of mutant superoxide dismutase 1 associates with neurotoxicity in familial amyotrophic lateral sclerosis. *J Neurosci*. 2005;25(1):108-17.
46. Rogov VV, et al. Structural and functional analysis of the GABARAP interaction motif (GIM). *EMBO Rep*. 2017;18(8):1382-96.
47. Magnus CJ, et al. Chemical and genetic engineering of selective ion channel-ligand interactions. *Science*. 2011;333(6047):1292-6.

48. Ouali Alami N, et al. Multiplexed chemogenetics in astrocytes and motoneurons restore blood-spinal cord barrier in ALS. *Life Sci Alliance*. 2020;3(11).
49. Etkin A, et al. A role in learning for SRF: deletion in the adult forebrain disrupts LTD and the formation of an immediate memory of a novel context. *Neuron*. 2006;50(1):127-43.
50. Bell RD, et al. SRF and myocardin regulate LRP-mediated amyloid-beta clearance in brain vascular cells. *Nat Cell Biol*. 2009;11(2):143-53.
51. Chow N, et al. Serum response factor and myocardin mediate arterial hypercontractility and cerebral blood flow dysregulation in Alzheimer's phenotype. *Proc Natl Acad Sci U S A*. 2007;104(3):823-8.
52. Knöll B, et al. Serum response factor controls neuronal circuit assembly in the hippocampus. *Nat Neurosci*. 2006;9(2):195-204.
53. Li CL, et al. SRF phosphorylation by glycogen synthase kinase-3 promotes axon growth in hippocampal neurons. *J Neurosci*. 2014;34(11):4027-42.
54. Lu PP, and Ramanan N. A critical cell-intrinsic role for serum response factor in glial specification in the CNS. *J Neurosci*. 2012;32(23):8012-23.
55. Wickramasinghe SR, et al. Serum response factor mediates NGF-dependent target innervation by embryonic DRG sensory neurons. *Neuron*. 2008;58(4):532-45.
56. Seijffers R, et al. ATF3 expression improves motor function in the ALS mouse model by promoting motor neuron survival and retaining muscle innervation. *Proc Natl Acad Sci U S A*. 2014;111(4):1622-7.
57. Catanese A, et al. Synaptic disruption and CREB-regulated transcription are restored by K(+) channel blockers in ALS. *EMBO Mol Med*. 2021;13(7):e13131.
58. Pandey K, et al. Autophagy coupled to translation is required for long-term memory. *Autophagy*. 2021;17(7):1614-35.
59. Zhang T, et al. NPAS4 suppresses propofol-induced neurotoxicity by inhibiting autophagy in hippocampal neuronal cells. *Arch Biochem Biophys*. 2021;711:109018.
60. Cheng X-Y, et al. Serum Response Factor Promotes Dopaminergic Neuron Survival via Activation of Beclin 1-Dependent Autophagy. *Neuroscience*. 2018;371:288-95.
61. Luo J, et al. Regulation of SRF protein stability by an autophagy-dependent pathway. *Biochem Biophys Res Commun*. 2020;521(2):279-84.
62. Goode A, et al. Defective recognition of LC3B by mutant SQSTM1/p62 implicates impairment of autophagy as a pathogenic mechanism in ALS-FTLD. *Autophagy*. 2016;12(7):1094-104.
63. Valenzuela V, et al. Unraveling the role of motoneuron autophagy in ALS. *Autophagy*. 2018;14(4):733-7.
64. Harding O, et al. ALS- and FTD-associated missense mutations in TBK1 differentially disrupt mitophagy. *Proc Natl Acad Sci U S A*. 2021;118(24).
65. Bamburg JR, et al. ADF/Cofilin-actin rods in neurodegenerative diseases. *Curr Alzheimer Res*. 2010;7(3):241-50.
66. Munsie LN, et al. Cofilin nuclear-cytoplasmic shuttling affects cofilin-actin rod formation during stress. *J Cell Sci*. 2012;125(Pt 17):3977-88.
67. Gunes ZI, et al. Exciting Complexity: The Role of Motor Circuit Elements in ALS Pathophysiology. *Front Neurosci*. 2020;14:573.
68. King AE, et al. Excitotoxicity in ALS: Overstimulation, or overreaction? *Exp Neurol*. 2016;275 Pt 1:162-71.
69. Durand J, et al. Hypoexcitability of Motoneurons: An Early Pathological Sign in ALS. *Neuroscience*. 2021;465:233-4.
70. Sareen D, et al. Targeting RNA foci in iPSC-derived motor neurons from ALS patients with a C9ORF72 repeat expansion. *Sci Transl Med*. 2013;5(208):208ra149.
71. Jensen BK, et al. Synaptic dysfunction induced by glycine-alanine dipeptides in C9orf72-ALS/FTD is rescued by SV2 replenishment. *EMBO Mol Med*. 2020;12(5):e10722.
72. Perkins EM, et al. Altered network properties in C9ORF72 repeat expansion cortical neurons are due to synaptic dysfunction. *Mol Neurodegener*. 2021;16(1):13.
73. Alberti S, et al. Neuronal migration in the murine rostral migratory stream requires serum response factor. *Proc Natl Acad Sci U S A*. 2005;102(17):6148-53.

74. Meyer Zu Reckendorf S, et al. Motoneuron-Specific PTEN Deletion in Mice Induces Neuronal Hypertrophy and Also Regeneration after Facial Nerve Injury. *J Neurosci*. 2022;42(12):2474-91.
75. May S, et al. C9orf72 FTLD/ALS-associated Gly-Ala dipeptide repeat proteins cause neuronal toxicity and Unc119 sequestration. *Acta Neuropathol*. 2014;128(4):485-503.

Figures **legends**

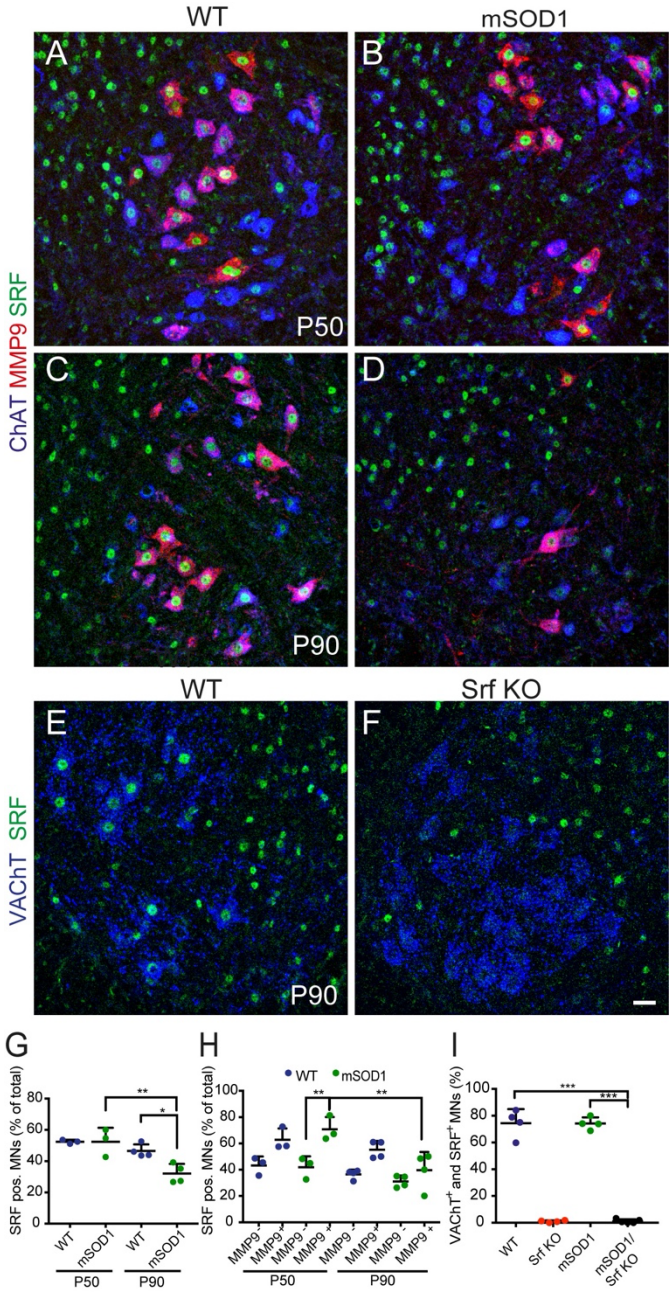

Figure 1
SRF is present in vulnerable MNs

(A-D) Ventral horns from P50 (A, B) or P90 (C, D) WT (A, C) or mSOD1 (B, D) mice were stained for ChAT (blue), MMP9 (red) and SRF (green). SRF is present in non-vulnerable MMP9 negative and vulnerable MMP9 positive MNs in WT and mSOD1 mice.

(E, F) In Srf KO MNs (F), SRF was absent from VAChT positive MNs at P90 in contrast to WT MNs (E).

(G) In WT and mSOD1 mice, approximately 50% of MNs were SRF positive at P50. At P90, abundance of SRF positive MNs was decreased in mSOD1 mice. There was no significant change in WT MNs between P50 and P90.

(H) In WT mice, SRF was more present in MMP9 positive MNs (approx. 60%) compared to MMP9 negative MNs (approx. 40%). In mSOD1 mice, SRF was significantly more present in vulnerable MMP9 positive MNs compared to MMP9 negative MNs at P50, in contrast to P90.

(I) SRF was nearly absent from MNs in Srf KO and SOD1/Srf KO mice compared to WT and SOD1 animals at P90.

In (G-I) N Numbers are provided by colored dots, each reflecting one mouse. N numbers (G, H) = 486 MNs (WT, P50), 377 MNs (mSOD1, P50); 512 MNs (WT, P90), 411 MNs (mSOD1, P90); (I) = 598 MNs (WT), 558 MNs (Srf KO), 584 MNs (mSOD1) and 650 MNs (mSOD1/Srf KO). Statistical testing was performed by one-way ANOVA with Tukey corrections.

Scale-bar (A-F) = 30 µm

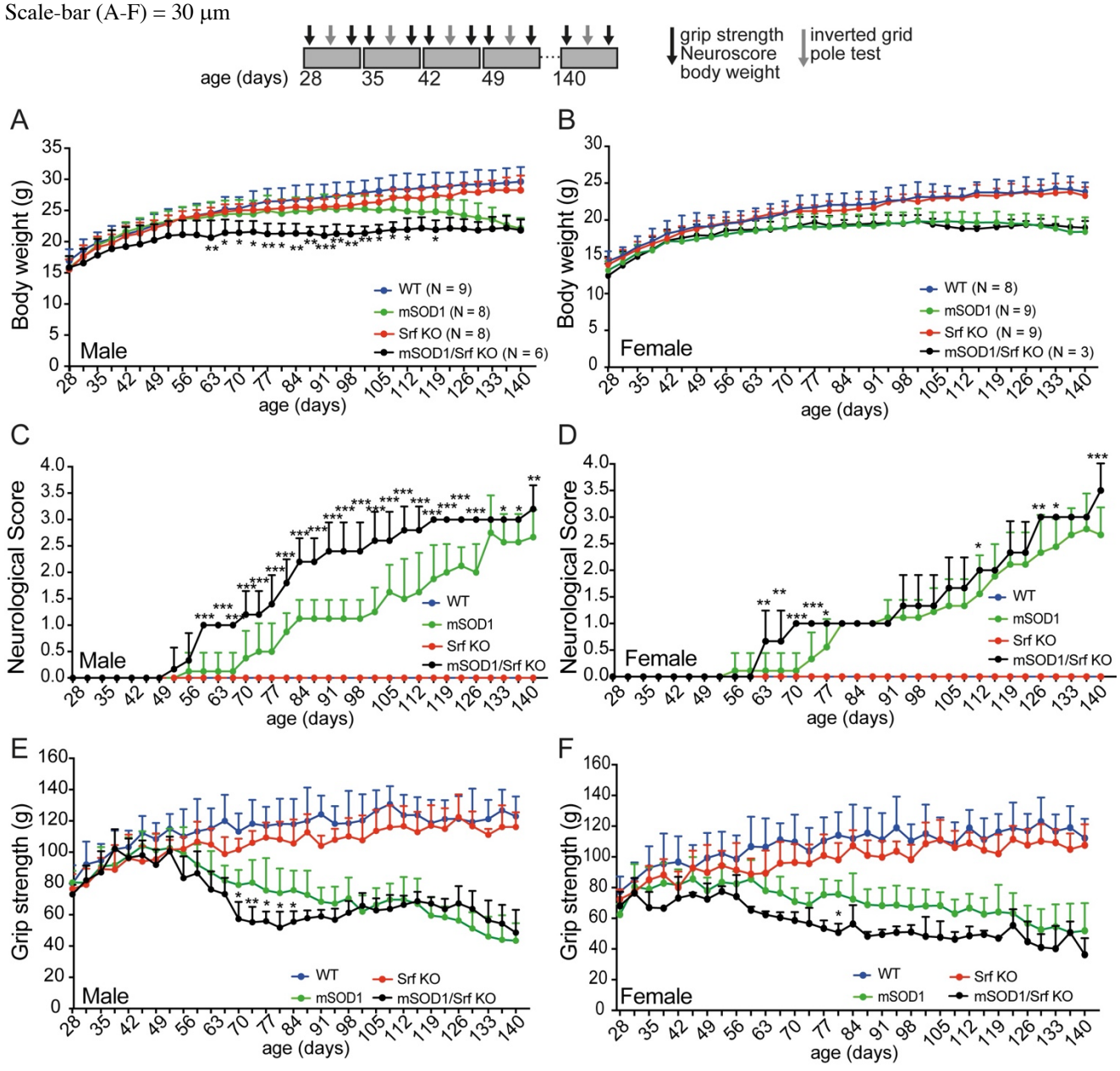

Figure 2

SRF deletion results in earlier disease onset in the SOD1 mouse model

Animals were analyzed weekly from 28 to 140 days of age. In each week, grip-strength, NeuroScore and body-weight were determined twice and inverted grid and pole test were performed once.

(A, B) In male mSOD1/Srf KO mice (A) a decrease in body-weight was observed earlier compared to mSOD1 mice. This was not observed in female mice (B).

(C, D) The NeuroScore showed an earlier elevation in male mSOD1/Srf KO mice compared to mSOD1 mice (C). A similar phenotype was observed in female mSOD1/Srf KO mice (D).

(E, F) The grip strength of the forelimbs was decreased in both male (E) and female (F) mSOD1/Srf KO mice compared to mSOD1 mice starting at approximately 8 weeks.

N numbers of animals are indicated in (A, B). Statistical testing was performed by two-way ANOVA with Tukey corrections.

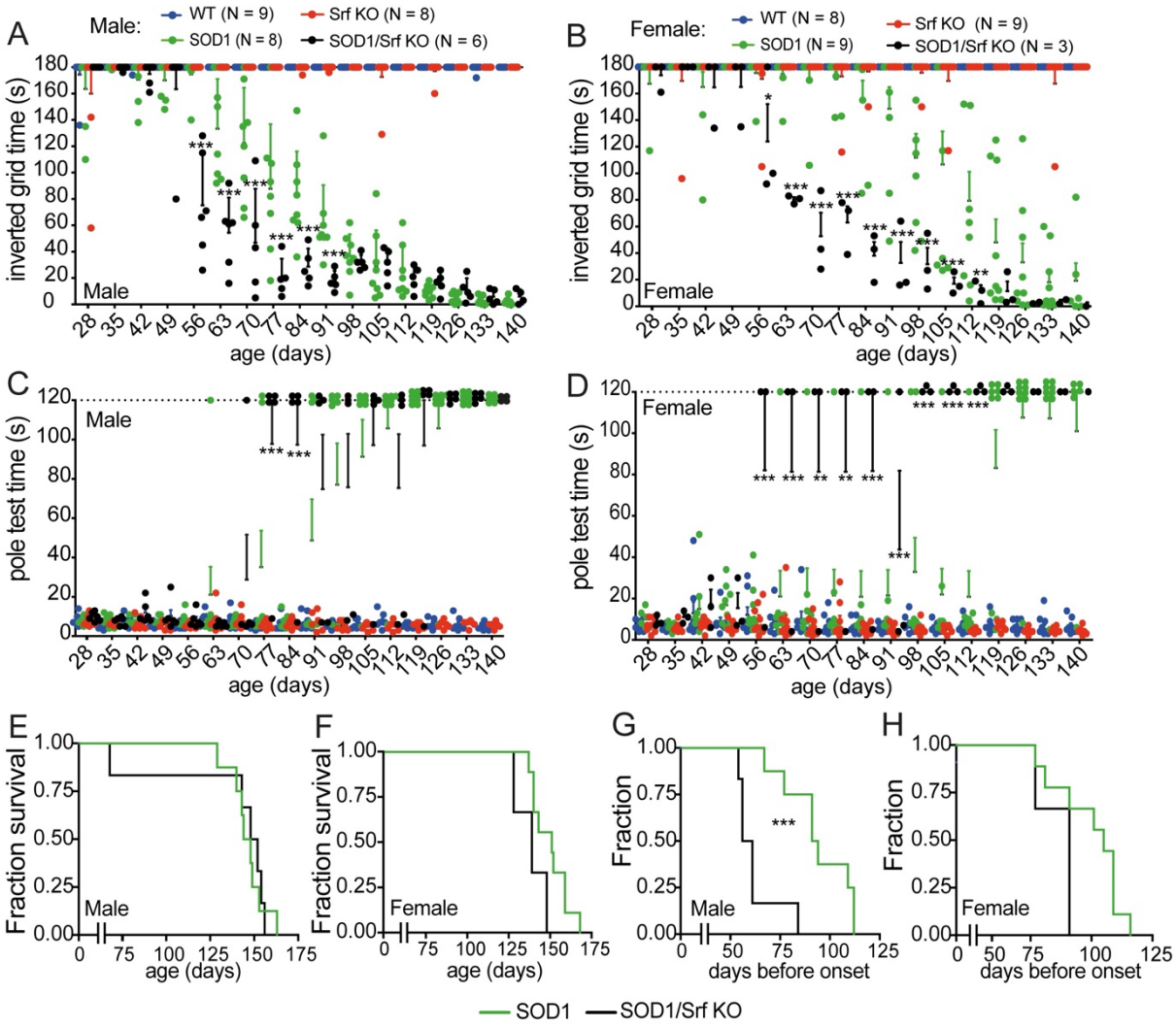

Figure 3

SRF deletion results in earlier motor impairments in SOD1 mice

(A, B) Male (A) and female (B) mSOD1/Srf KO mice dropped down earlier in the inverted grid test compared to mSOD1 mice. WT and Srf KO mice held on for 180 seconds.

(C, D) In the pole test, male (C) and female (D) mSOD1/Srf KO mice could not climb down the pole as quickly as mSOD1 mice. In contrast, WT and Srf KO mice climbed down within 10 seconds. This data is presented as mean ± SEM.

(E, F) The survival of male (E) or female (F) mSOD1/Srf KO mice was comparable to mSOD1 mice.

(G, H) The disease onset calculated on the basis of the body-weight curves was earlier in male mSOD1/Srf KO mice compared to mSOD1 mice (G). In female mice, the same tendency was observed (H).

In (A-D) each colored dot reflects one mouse. N numbers of animals are indicated in (A, B). Statistical testing was performed by two-way ANOVA with Tukey corrections (A-D) and Mantel-Cox test (E-H).

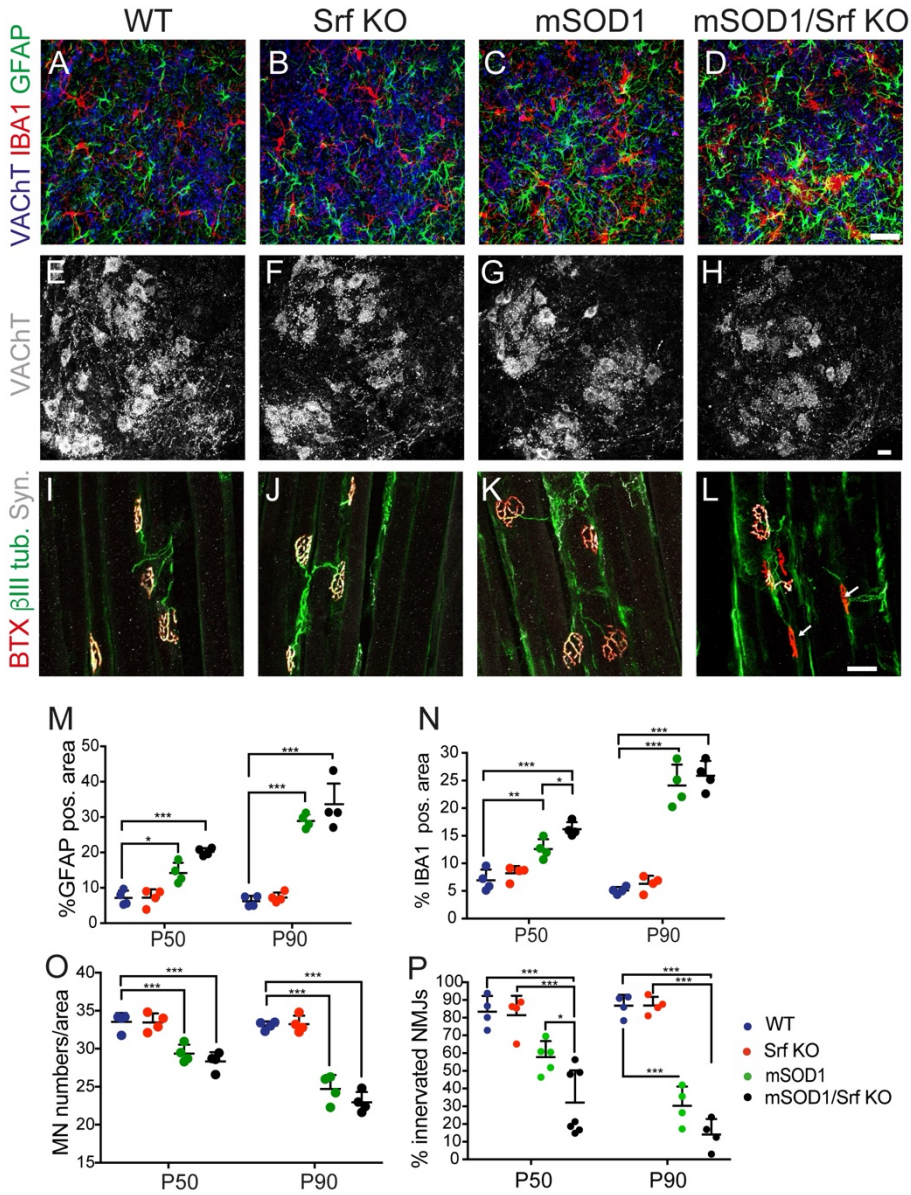

Figure 4

SRF deletion enhances microgliosis and accelerates neuromuscular junction denervation

(A-D) Ventral horns from P50 WT (A), Srf KO (B), mSOD1 (C) and mSOD1/Srf KO (D) mice were stained for VAChT (blue), microglia (IBA1; red) and astrocytes (GFAP; green). In mSOD1/Srf KO mice, microglia and less pronounced astrocyte abundance was elevated compared to other cohorts (see M, N).

(E-H) The MN number in ventral horns labelled with VAChT was reduced in mSOD1 (G) and mSOD1/Srf KO (H) compared to WT (E) and Srf KO (F) mice. However, no differences between mSOD1 (G) and mSOD1/Srf KO (H) cohorts were discernible.

(I-L) In mSOD1/Srf KO mice (L), a reduction in NMJ innervation was observed (see NMJs marked with arrows).

(M, N) Quantification of GFAP (M) and IBA1 (N) abundance in P50 and P90 mice.

(O) The MN number was reduced in mSOD1 and mSOD1/Srf KO cohorts at P50 and more pronounced at P90 compared to WT and Srf KO mice.

(P) In mSOD1/Srf KO mice, the percentage of innervated NMJs was decreased significantly at P50 and with the same tendency at P90 in relation to mSOD1 mice.

In (M-P) N numbers are indicated by each colored dot reflecting one mouse. In (O) N numbers of MNs/sections analyzed were for P50 as follows: 1483/44 (WT), 1713/51 (Srf KO), 1484/50 (mSOD1), 1428/50 (mSOD1/Srf KO). For P90: 1322/40 (WT), 1330/40 (Srf KO), 988/40 (mSOD1), 940/41 (mSOD1/Srf KO). In (P) N numbers for NMJ were for P50, 462 (WT), 432 (Srf KO), 472 (mSOD1), 834 (mSOD1/Srf KO) and for P90, 456 (WT), 458 (Srf KO), 480 (mSOD1), 441 (mSOD1/Srf KO). Statistical testing was performed by one-way ANOVA with Tukey corrections.

Scale bar (A-D), (E-H), (I-L) = 30 µm

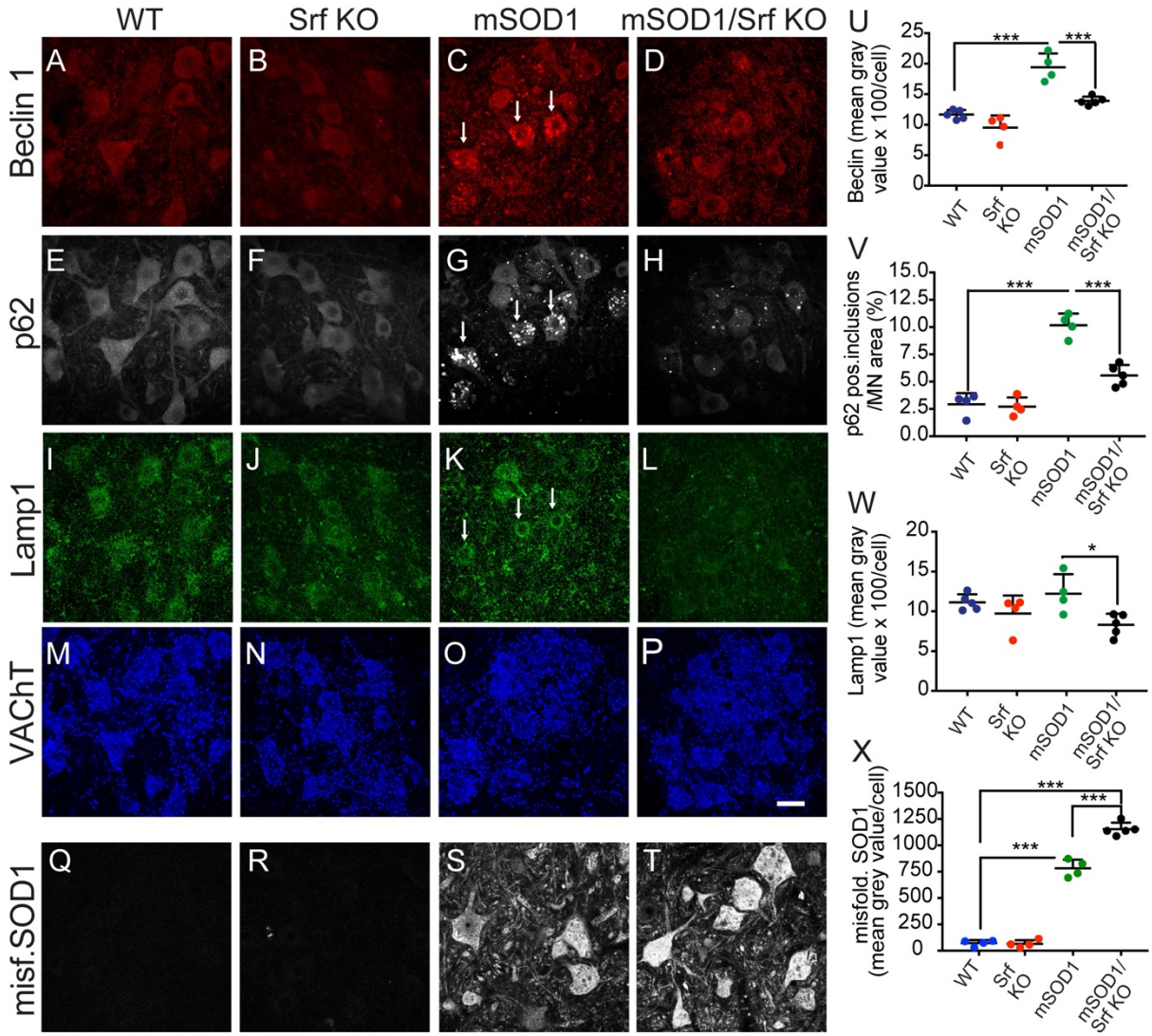

Figure 5

Reduced autophagy induction upon SRF deletion in SOD1 mice

(A-D) Beclin 1 abundance was upregulated in P50 ventral horns of mSOD1 (arrows in C) compared to WT (A) and Srf KO (B) mice. SRF deletion in SOD1 mice (D) reduced the Beclin1 abundance.

(E-H) p62 was upregulated in MNs of mSOD1 mice (arrows in G). In mSOD1/Srf KO mice p62 accumulation was diminished (H).

(I-L) Lamp1 was more abundant in mSOD1 mice (arrows in K) and this was reduced in mSOD1/Srf KO (L) mice.

(M-P) VAChT staining of all four cohorts in corresponding regions.

(Q-T) Misfolded SOD1 was absent from WT (Q) and SRF deficient (R) MNs, whereas accumulations were found in mSOD1 (S) and more pronounced in mSOD1/Srf KO (T) mice.

(U-X) Beclin1 (U), p62 (V) and Lamp1 (W) signals were induced in mSOD1 mice compared to WT mice. This was not observed to the same extent in mSOD1/Srf KO animals. Misfolded SOD1 was present in mSOD1 (S) and stronger in mSOD1/Srf KO MNs (T; X).

In (U-X) N numbers are indicated by each colored dot reflecting one mouse. In (U-W) N numbers for MNs analyzed were: 305 (WT), 293 (Srf KO), 287 (mSOD1) and 383 (mSOD1/Srf KO). In (X) MN numbers were as follows: 619 (WT), 682 (Srf KO), 413 (mSOD1), 400 (mSOD1/Srf KO). Statistical testing was performed by one-way ANOVA with Tukey corrections.

Scale bar (A-T) = 30 µm

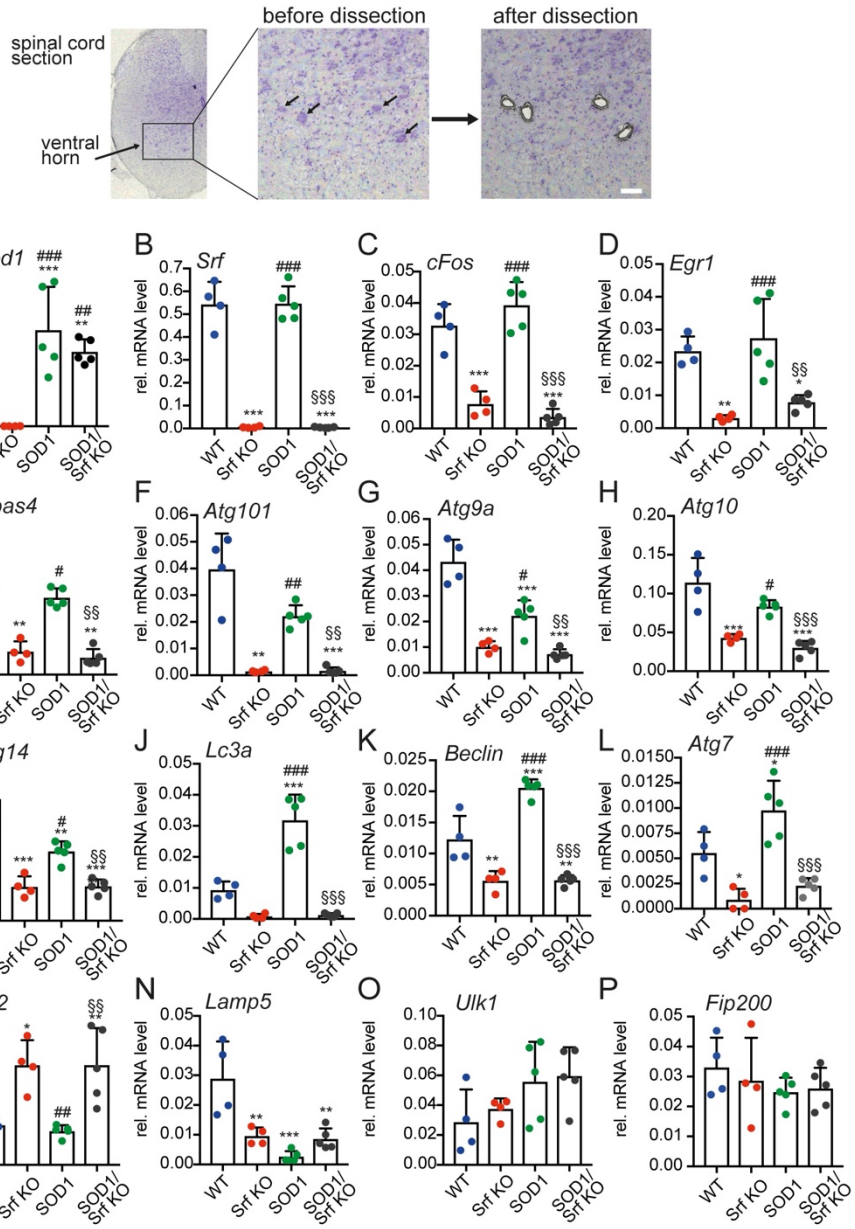

Figure 6

Reduced autophagy induction upon SRF deletion in SOD1 mice

MNs from the ventral horn of P50 mice were subjected to qPCR analysis. Arrows point at MNs before dissection. After dissection, MNs were selectively removed.

(A) The mRNA abundance of human *Sod1* was specifically increased in MNs of mSOD1 and mSOD1/Srf KO mice.

(B) *Srf* mRNA was removed from MNs of Srf KO and mSOD1/Srf KO animals.

(C-E) *cFos* (C), *Egr1* (D) and *Npas4* (E) were reduced in Srf KO animals and to a similar extent in mSOD1/Srf KO mice.

(F-I) In relation to WT, mRNA levels of *Atg101* (F) *Atg9*a (G), *Atg10* (H) and *Atg14* (I) were reduced in Srf KO and mSOD1 MNs. It is important to note that in mSOD1/Srf KO MNs, the mRNA levels of all four genes were lower compared to mSOD1 MNs.

(J-L) mRNA abundance of *Map1lc3a* (J), *Beclin1* (K) and *Atg7* (L) was reduced in Srf KO and upregulated in mSOD1 MNs in relation to WT. The upregulation of all three genes in mSOD1 MNs was not observed in mSOD1/Srf KO MNs.

(M) *p62* mRNA was not induced in Srf KO and mSOD1/Srf KO MNs in relation to WT and mSOD1 MNs.

(N) *Lamp5* abundance was downregulated in Srf KO, mSOD1 and mSOD1/Srf KO MNs in comparison to WT.

(O, P) *Ulk1* (O) and *Fip200* (P) abundance was not overtly changed between cohorts.

In (A-P) N number are indicated by each colored dot reflecting one mouse.

*, #, § denote significance in relation to WT, Srf KO and mSOD1 respectively. Statistical testing was performed by one way ANOVA with Tukey corrections.

Scale bar = 30 μm

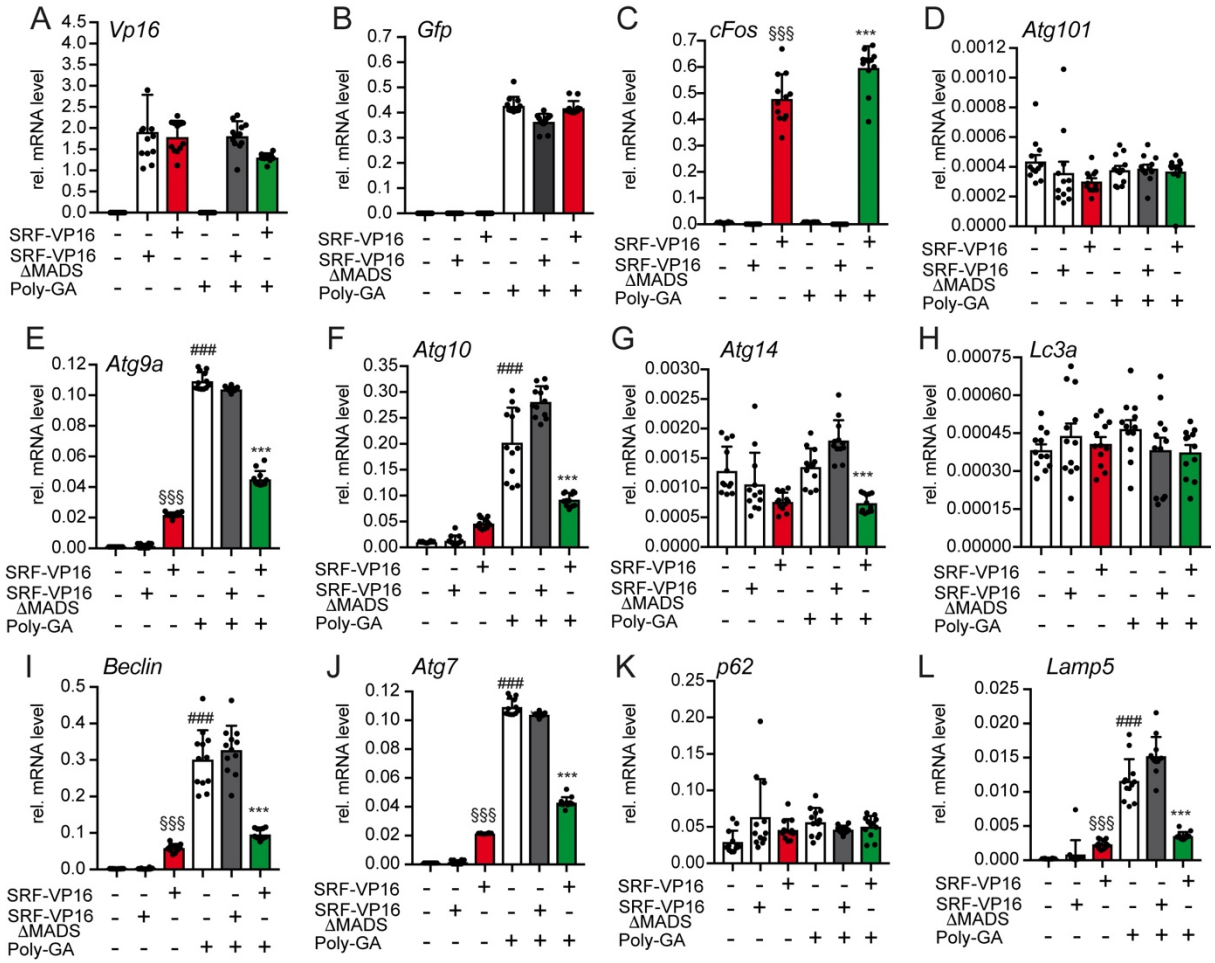

Figure 7

SRF-VP16 reduces C9orf72 associated induction of autophagy genes

HEK293 cells expressed either constitutively-active SRF-VP16 or inactive SRF-VP16ΔMADS in the presence or absence of aggregates formed by Poly-GA expression. Subsequently, qPCR was performed to assess mRNA abundance of the genes indicated.

(A-C) Expression of *Vp16* tagged SRF (A) and *Gfp* tagged Poly-GA (B) was similar on an mRNA level. SRF-VP16 but not SRF-VP16ΔMADS induced *cFos* (C).

(D-L) SRF-VP16 but not SRF-VP16ΔMADS induced *Atg9a* (E), *Atg10* (F), *Beclin* (I) and *Atg7* (J) as well as *Lamp5* (L). Poly-GA expression upregulated *Atg9a* (E), *Atg10* (F), *Beclin* (I), *Atg7* (J) and *Lamp5* (L) but not *Atg101* (D), *Atg14* (G), *Lc3a* (H) and *p61* (K). SRF-VP16 but not SRF-VP16ΔMADS down-regulated several of those autophagy and lysosome encoding genes induced by Poly-GA aggregate formation.

In (A-L) N Numbers are indicated by each black dot reflecting one cell culture dish.

*, #, § denote significance between SRF-VP16 and SRF-VP16ΔMADS in the presence of Poly-GA (5th and 6th bar), between mock and Poly-GA (1st and 4th bar) and between SRF-VP16 and SRF-VP16ΔMADS (2nd and 3rd bar), respectively. Statistical testing was performed by one way ANOVA with Tukey corrections.

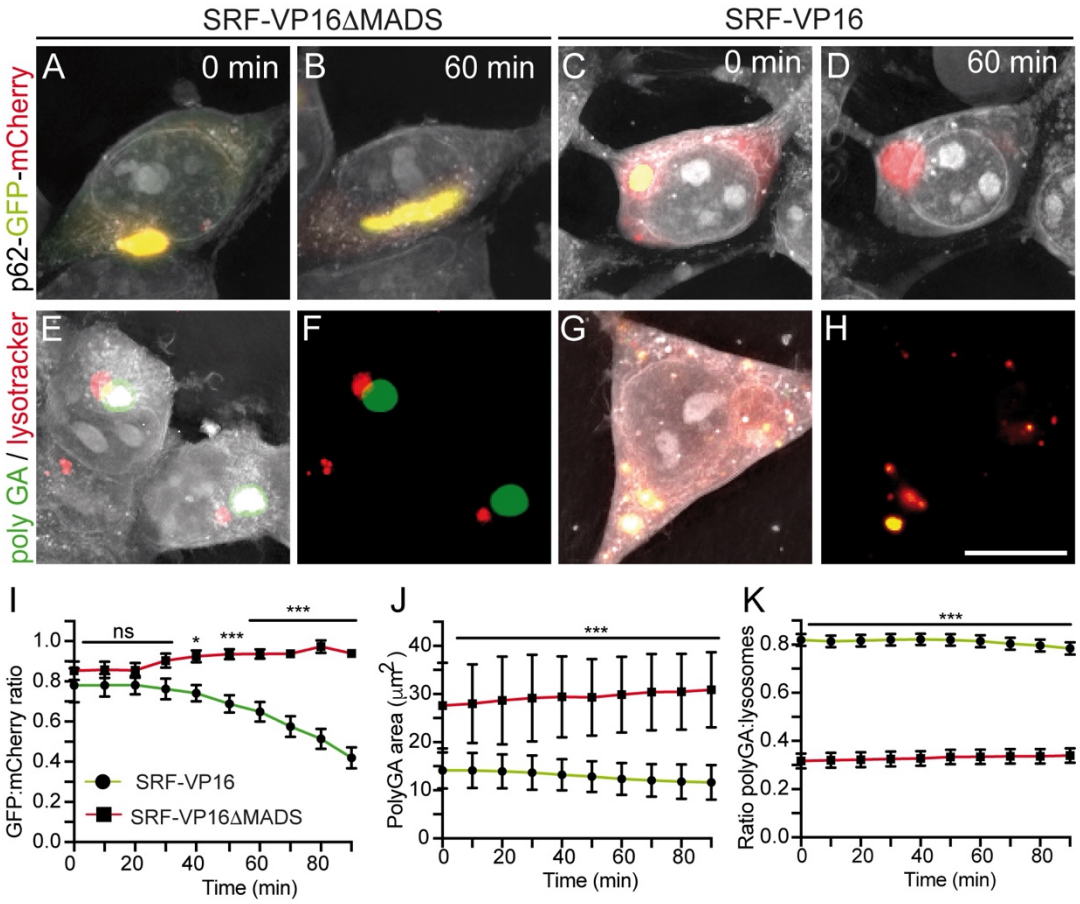

Figure 8

SRF-VP16 enhances autophagy Poly-GA aggregate clearance

(A-D) HEK293 cells transfected with a p62-GFP-mCherry construct co-expressed either SRF-VP16ΔMADS (A, B) or SRF-VP16 (C, D). Cells were imaged over 90 minutes and pictures show the starting timepoint (0 min; A, C) or 60 minutes (B, D). Enhanced autophagy is indicated by a color change from yellow to red. SRF-VP16 enhanced autophagy propagation as indicated by yellow vesicles at t=0 (C) turning at t=60 min into red (D). In SRF-VP16ΔMADS expressing cells the ratio between GFP:mCherry remained constant (A, B).

(E-H) HEK293 cells expressing Poly-GA aggregates (green) were stained with lysotracker (red). SRF-VP16 (G, H) but not as much SRF-VP16ΔMADS (E, F) reduced aggregate size and enhanced co-localization of aggregates with lysosomes (yellow in G, H).

(I) The GFP:mCherry ratio was decreased in SRF-VP16 compared to SRF-VP16ΔMADS expressing cells indicating enhanced autophagic flux by SRF-VP16 (N = 20 cells each; 3 technical replicates). Data show mean ± SEM.

(J) The area of Poly-GA aggregates was lower in SRF-VP16 compared to SRF-VP16ΔMADS expressing cells (N = 40 cells each). Data show mean ± SD.

(K) In SRF-VP16 expressing cells the Poly-GA:lysosome ratio was higher suggesting more co-localization of aggregates in lysosomes compared to SRF-VP16ΔMADS (N = 40 cells each; 4 technical replicates). Data show mean ± SEM.

Statistical testing was performed by T tests.

Scale-bar (A-H) = 10 μm

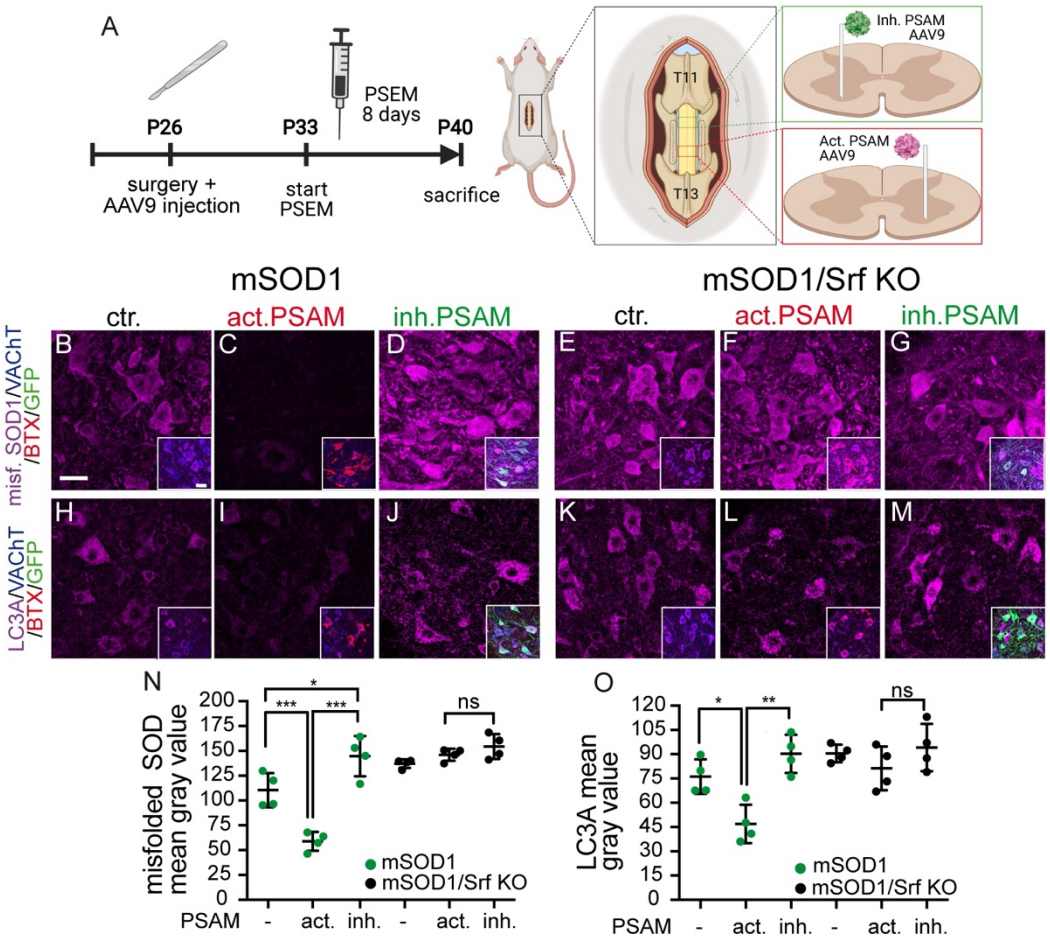

Figure 9

Chemogenetics reveals a requirement of SRF for neuronal activity to modulate disease burden in ALS affected MNs

(A) P26 mice were injected into the spinal cord (level T11-T13) with AAV9 particles driving inhibitory (inh. PSAM labelled with GFP in green) or activatory PSAM expression (act. PSAM labelled with BTX in red). At P33, mice were injected for eight days with the PSEM ligand. After sacrificing, ventral horns were stained for misfolded SOD1 and LC3A (along with VAChT, BTX and GFP). Diagram created with BioRender.com with agreement No. ON244OBBZ4.

(B-G) MNs of mSOD1 (B-D) or mSOD1/Srf KO (E-G) mice were stained for misf. SOD1 abundance. In mSOD1 mice, act. PSAM (C) lowered, whereas inh. PSAM (D) enhanced misf. SOD1 level compared to mock infection (ctr.; B). In mSOD1/Srf KO mice, chemogenetic manipulation failed to alter misf. SOD1 levels (E-G). Inserts in (B-G) show a merged picture of all channels.

(H-M) LC3A levels were decreased by act. PSAM (I) and slightly enhanced by inh. PSAM (J) compared to control (H) in mSOD1 mice. In SRF deleted mice, neuronal excitability did not change LC3A abundance (K-M). Inserts in (H-M) show a merged picture.

(N, O) Quantification of mean gray values for misfolded SOD1 (N) or LC3A (O). In (N, O) N Numbers are indicated by dots each reflecting one animal. In (N) N numbers for MNs in mSOD1 mice were 150 (PSAM neg.), 198 (act. PSAM) and 200 (inh. PSAM) and for mSOD1/Srf KO mice 148 (PSAM neg.), 150 (act. PSAM) and 200 (inh. PSAM). In (O) N numbers for MNs in mSOD1 mice were 153 (PSAM neg.), 200 (act. PSAM) and 200 (inh. PSAM) and for mSOD1/Srf KO mice 191 (PSAM neg.), 150 (act. PSAM) and 200 (inh. PSAM).

Statistical testing was performed by one-way ANOVA with Tukey corrections.

Scale-bar (B-M) = 30 µm

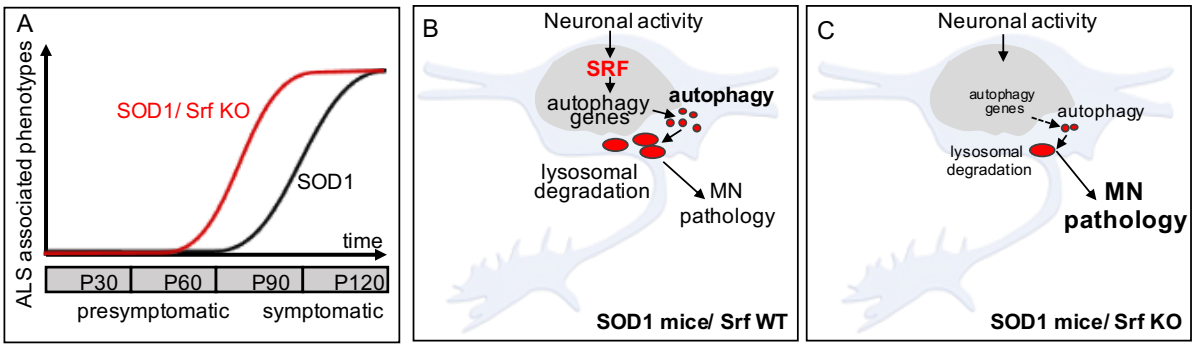

Figure 10

SRF connects neuronal activity mediated gene transcription with autophagy in ALS MNs

(A) In mSOD1 mice with SRF (black line), ALS associated phenotypes such as body-weight loss and impaired motor function appeared at around P90. This disease onset was shifted to approximately P50 in mSOD1 mice with SRF deletion (mSOD1/Srf KO; red line). At the disease endpoint, both cohorts were similar.

(B) In mSOD1 mice, neuronal activity activates SRF mediated gene transcription resulting in autophagic gene induction in MNs. This might facilitate removal of inclusions through autophagy and lysosomes, thereby improving neuronal survival.

(C) In mSOD1/Srf KO mice, loss of SRF limits the induction of an autophagy program by neuronal activity, thereby precipitating MN vulnerability. This contributes to impaired MN function and, subsequently, a premature disease onset.